

Simulations of starspot anomalies within TESS exoplanetary transit light curves – I.

The detection limits of starspot anomalies in TESS light curves

J. Tregloan-Reed¹ and E. Unda-Sanzana¹

Centro de Astronomía (CITEVA), Universidad de Antofagasta, Avenida U. de Antofagasta 02800, Antofagasta, Chile
 e-mail: jeremy.tregloanreed@uantof.cl

Received April 19, 2019; accepted August 14, 2019

ABSTRACT

Context. The primary targets of the NASA *Transiting Exoplanet Survey Satellite* will be K and M dwarf stars within our solar neighbourhood. Young K and M dwarf stars are known to exhibit a high starspot coverage ($\approx 50\%$), however, older stars are known to show fewer starspots. This implies that TESS 2 min cadence transit light curves may contain starspot anomalies, and if so, will require transit-starspot models to accurately determine the properties of the system.

Aims. The goals are to determine if starspot anomalies can manifest in TESS transit light curves, to determine the detection limits of the starspot anomalies and to examine the relationship between the change in flux caused by the starspot anomaly and the planetary transit.

Methods. 20573 simulations of planetary transits around spotted stars were conducted using the transit-starspot model, PRISM. In total 3888 different scenarios were considered using three different host star spectral types, M4V, M1V and K5V. The mean amplitude of the starspot anomaly was measured and compared to the photometric precision of the light curve, to determine if the starspot anomaly’s characteristic “blip” was noticeable in the light curve.

Results. The simulations show that, starspot anomalies will be observable in TESS 2 min cadence data. The smallest starspot detectable in TESS transit light curves has a radius of ≈ 1900 km. The starspot detection limits for the three host stars are: 4900 ± 1700 km (M4V), 13800 ± 6000 km (M1V) and 15900 ± 6800 km (K5V). The smallest change in flux of the starspot ($\Delta F_{\text{spot}} = 0.00015 \pm 0.00001$) can be detected when the ratio between the planetary and stellar radii, $k = 0.082 \pm 0.004$.

Conclusions. The results confirm known dependencies between the amplitude of the starspot anomaly and the photometric parameters of the light curve. The results allowed the characterisation of the relationship between the change in flux of the starspot anomaly and the change in flux of the planetary transit for TESS transit light curves.

Key words. Stars: late-type – Stars: activity – Stars: starspots – Planets and satellites – Methods: numerical – Techniques: photometric

1. Introduction

The next generation of transit planet hunters (e.g., Next Generation Transit Survey: Wheatley et al. 2013; NASA *Transiting Exoplanet Survey Satellite*: Ricker et al. 2009, 2014, 2015) will observe transiting planets orbiting both K and M dwarf stars, within, the solar neighbourhood (with an emphasis on super-Earth: $1.25 R_{\oplus}$ to $2 R_{\oplus}$; sub-Neptune: $2 R_{\oplus}$ to $4 R_{\oplus}$; Neptune: $4 R_{\oplus}$ to $6 R_{\oplus}$ class planets). TiO absorption bands show that young K dwarfs can have 20-40% starspot coverage (O’Neal et al. 2004), while young M dwarfs can have a starspot coverage of $40 \pm 10\%$ (Jackson & Jeffries 2013). Older stars are known to show fewer starspots, however, the dependence on age has not been reliably quantified. This leads to the potential of an increased likelihood that the transits observed by these new planet hunters, will contain starspot anomalies.

Late-type stars (G, K, M) have magnetic fields, which often manifest themselves as dark spots on the stellar surface. When a transiting planet passes in front of a starspot, a short-term increase in the brightness of the star is seen because the planet is temporarily blocking a fainter part of the star’s surface (Silva 2003). This “blip” in the light

curve can be modelled to determine the size and position of the starspot (e.g., WASP-19: Tregloan-Reed et al. 2013; Mancini et al. 2013; WASP-6: Tregloan-Reed et al. 2015; CoRoT-2: Silva-Valio et al. 2010; WASP-4: Sanchis-Ojeda et al. 2011; HAT-P-11: Sanchis-Ojeda & Winn 2011; Kepler-30: Sanchis-Ojeda et al. 2012; Kepler-63: Sanchis-Ojeda et al. 2013; HATS-2: Mohler-Fischer et al. 2013; Qatar-2: Mancini et al. 2014; WASP-41: Southworth et al. 2016; WASP-52: Mancini et al. 2017; GJ 3470: Chen et al. 2017; Kepler-17: Valio et al. 2017).

Starspots can affect the shape of the light curve (Silva-Válío 2010) and if not correctly modelled can lead to biased measurements of the system parameters (e.g., planetary radius: Nikolov et al. 2013; limb darkening coefficients: Ballerini et al. 2012; time of minimum light: Sanchis-Ojeda et al. 2011). However, if the perturbations are accounted for then an accurate measurement of the planetary radius will be achievable, improving investigations into the atmosphere, structure and evolution of a planet (Fortney et al. 2007).

When two closely spaced transit light curves, both of which contain a starspot anomaly (due to the same starspot), are accurately modelled, the position of the starspot can be determined at

two distinct points in time, allowing an extraction of the latitudinal stellar rotation period (P_*) and sky-projected orbital obliquity (the sky projection of the angle between the orbit of the planet and the spin of the host star), λ from the transit light curves (e.g., Sanchis-Ojeda et al. 2011; Sanchis-Ojeda & Winn 2011; Tregloan-Reed et al. 2013, 2015; Southworth et al. 2016; Mancini et al. 2017).

Over the years there have been multiple transit-starspot models developed both by the eclipsing binary star community (e.g., Wilson-Devinney code: Wilson & Devinney 1971; Wilson 1979, 1990, 2008, 2012; PHEOBE: Prša & Zwitter 2005; Prša et al. 2016) and the exoplanet community (e.g., PRISM: Tregloan-Reed et al. 2013, 2015, 2018; SOAP-T: Oshagh et al. 2013; spotrod: Béky et al. 2014; KSint: Montalto et al. 2014; ellc: Maxted 2016; StarSim: Herrero et al. 2016; PyTranSpot: Juvan et al. 2018). With a large variety of models readily available to the community, the treatment of starspot anomalies and their associated effects on light curves, no longer cause difficulties or delays in the analysis of the exoplanetary light curves.

Locating starspot anomalies in light curves of smaller planets requires a significantly higher precision in the light curve because the size of the starspot anomaly scales linearly with the area of the planetary disc (Tregloan-Reed et al. 2013). This precludes the use of ground-based data for small planets, but the remarkable quality of the light curves from dedicated space missions such as the *Kepler* satellite (Borucki et al. 2010) makes this work viable. Whilst the temporal sampling of *Kepler* data (30 min cadence) is too low to resolve starspot anomalies for the vast majority of the stars observed, the NASA *Transiting Exoplanet Survey Satellite* (TESS) will observe $\geq 200,000$ stars at a 2 min cadence (Stassun et al. 2018) and provide a large set of light curves suitable for detecting and measuring starspots.

TESS will spend two years looking for super-Earth planets ($< 2R_\oplus$) transiting between 200,000 and 400,000 pre-selected stars at a cadence of two minutes, (Stassun et al. 2018) with a particular emphasis on M dwarf stars. Recent simulations for TESS indicate the potential to detect 1700 planets from the smallest selection of pre-selected stars (Sullivan et al. 2015, 2017). With 1100 of these planets predicted to be sub-Neptune ($2R_\oplus$ to $4R_\oplus$) class planets, while, 419 super-Earth or smaller ($< 2R_\oplus$) planets, are expected to be found orbiting M dwarfs. With a further 137 super-Earth or smaller planets orbiting F, G, K stars (Sullivan et al. 2015, 2017). TESS is already exceeding early expectations with 21 confirmed planets (e.g., Pi Men-sae c: Huang et al. 2018; LHS 3884 b; Vanderspek et al. 2019; HD 21749 b; Dragomir et al. 2018; HD 202772A b; Wang et al. 2019) with a further 336 TESS Objects of Interest (ToIs)¹.

The objective of this work is to determine the detection limits of starspot anomalies in TESS exoplanetary transit light curves. This is accomplished by varying the variables that directly or indirectly alter the duration and/or amplitude of the starspot anomaly in the light curve, and compare the results against the photometric noise of the light curve: starspot size (r_{spot}) and temperature (T_{spot}), host star radius (R_*) and effective temperature (T_{eff}), planetary radius (R_p), semi-major axis (a), orbital period (P), orbital inclination (i), observing cadence and the frequency (ν) of the observation. Through this, it will be possible to determine the physical properties of starspots at the detection limits for TESS transit light curves.

The outline of this paper is as follows. Section 2 describes how the contrast of the starspots was calculated in the TESS

passband, for use in the simulations and describes which parameters influence the size and shape of the starspot anomalies. The section then describes how the simulations were designed using the PRISM model, to produce the simulated light curves. Section 3 presents the results, separated into three host star spectral types; K5V dwarf, M1V and M4V dwarf stars. Section 4 discusses the results and gives the overall conclusions to the simulations.

2. Simulating starspot anomalies with PRISM

The transit-starspot model PRISM (Tregloan-Reed et al. 2013, 2015, 2018) was used to perform the simulations in this work. PRISM² is written in IDL³ (Interactive Data Language) and uses a pixellation approach to model the stellar disc in a two-dimensional array, by subdividing the star into many individual elements. These elements can then be described by a two-dimensional vector in Cartesian coordinates. Each element is then assigned an intensity value based on if a stellar feature is present at that location and then applying the quadratic limb darkening law over the entire stellar disc. The planet is then set to transit the star. For each data point in the transit light curve, the total received intensity is calculated based on which elements of the star are visible. The pixellation method is an ideal method for introducing stellar features to the stellar disc because the model allows individual intensities to be assigned to individual elements at specific coordinates (see Tregloan-Reed et al. 2013). This allows researchers to use PRISM to model both occulted and unocculted starspots, and so, help “rule-out” starspot trends when examining wavelength dependent transit depth (planetary radii) variations.

The original version of PRISM used six parameters to model the light curve; ratio between the planetary and stellar radii (k), sum of the fractional ($r_p = R_p/a$ and $r_* = R_*/a$) planetary and stellar radii ($r_p + r_*$), linear and quadratic coefficients of the quadratic limb darkening law (u_1 and u_2), orbital inclination (i) and time of minimum light (T_0). Combined with four additional parameters for each starspot; longitude of the spot’s centre (θ), co-latitude of the spot’s centre (ϕ), angular size (r_{spot}) and contrast, the surface brightness of the starspot versus the immaculate photosphere (ρ_{spot}) (Tregloan-Reed et al. 2013). Since its publication, PRISM has had two major updates. The first added two orbital parameters; orbital eccentricity (e) and argument of periastron (ω) (Tregloan-Reed et al. 2015). The second major update included a third light parameter and the out-of-transit detrending polynomial coefficients (Tregloan-Reed et al. 2018).

During its development PRISM’s ability to model the stellar disc and transit was tested by using JKTEBOP (Southworth et al. 2004, 2005, 2007; Southworth 2008; Southworth et al. 2009; Southworth 2010, 2011, 2013) as a benchmark transit modelling program. For this a series of light curves were generated by both PRISM and JKTEBOP using the same transit parameter values. The average difference between the two models for all the tests was ~ 10 ppm, six times lower than the expected noise floor in TESS data (see Sullivan et al. 2015).

Since the development of PRISM other researchers have used the model to ascertain the photometric parameters of a transiting system and derive the parameters of the detected starspots observed in transit light curves (e.g., Mancini et al. 2013, 2014; Mohler-Fischer et al. 2013; Chen et al. 2017). PRISM has

¹ From TESS data MAST page; accessed 2019-06-24.

² The latest version of PRISM is available from GitHub

³ For further details see <http://www.harrisgeospatial.com/Productsand>

also been used to help calibrate and benchmark other transit-starspot models (e.g., *spotrod*: Béky et al. 2014; *PyTranSpot*: Juvan et al. 2018).

PRISM measures r_{spot} in units of angular radius ($^\circ$). Consequently, an n° starspot maintains a constant ratio between the stellar and starspot surfaces, for all values of R_* . The simulations in this work use three different host stars, and as such, three different R_* . To avoid the projection effects on the spherical surface of the star we quote the starspot stellar surface radius, in units of R_* , where:

$$n^\circ \equiv n^\circ \left(\frac{\pi}{180^\circ} \right) R_*, \quad (1)$$

where a starspot with an angular radius of 1° has a stellar surface radius of $0.017R_*$.

2.1. Typical starspot contrast in the TESS passband

While the temperature of the starspot (T_{spot}) is fixed across all wavelengths, ρ_{spot} is not, it is dependent on the frequency of the observation, ν . At bluer wavelengths ρ_{spot} reduces (higher contrast), increasing the amplitude of the starspot anomaly. This is because a starspot is cooler than the surrounding photosphere and both the starspot and photosphere can be treated as black bodies (Rabus et al. 2009; Sanchis-Ojeda & Winn 2011). When the observation wavelength shifts towards a redder wavelength, ρ_{spot} increases (lower contrast), and so, the amplitude of the starspot anomaly can potentially fade into the observational noise.

Assuming that both the starspot and surrounding photosphere radiate as blackbodies, Silva (2003) uses the ratio between the intensities of the starspot and surrounding photosphere to give an equation to find ρ_{spot} from the stellar effective temperature (T_{eff}), T_{spot} and ν . By doing so, Silva (2003) incorporates the spectral signature of the starspot into ρ_{spot} :

$$\rho_{\text{spot}} = \frac{\exp(h\nu/k_B T_{\text{eff}}) - 1}{\exp(h\nu/k_B T_{\text{spot}}) - 1}, \quad (2)$$

where h is Planck's constant and k_B is Boltzmann constant.

TESS will use its own T (TESS) passband with a spectral response between 600–1000 nm with the Johnson-Cousins I_C passband lying near the centre of the T -passband (Sullivan et al. 2015). The effective wavelength midpoint of the I_C passband lies approximately at 785 nm. Because a large proportion of the emitted flux from an M dwarf lies within the optical red-infrared (potentially engulfing the starspot signal due to the redder observational wavelengths) Eq. 2 was used to calculate the contrast for a typical starspot on a cool M dwarf at 600 nm, 785 nm and 1000 nm. Using a $T_{\text{eff}} = 3200$ K (transit detection limit in T passband; Sullivan et al. 2015) and setting T_{spot} to be 200 K cooler than the photosphere (i.e., $T_{\text{spot}} = 3000$ K), in-line with starspot temperatures of fully convective M dwarf stars (e.g., Barnes et al. 2015), ρ_{spot} was calculated to be $\rho_{\text{spot}} = 0.60$, $\rho_{\text{spot}} = 0.68$ and $\rho_{\text{spot}} = 0.74$ for the three respective wavelengths. The amplitude of a starspot anomaly is primarily dependent on r_{spot} and ρ_{spot} . However, there will be a critical threshold for ρ_{spot} where the starspot anomaly will no longer be detected, irrespective of r_{spot} . Previous work using ground-based telescopes, have found starspot anomalies with $\rho_{\text{spot}} > 0.74$ (e.g., HAT-P-36, $\rho_{\text{spot}} = 0.92$: Mancini et al. 2015; WASP-41, $\rho_{\text{spot}} = 0.90$: Southworth et al. 2016; WASP-6,

$\rho_{\text{spot}} = 0.80$: Tregloan-Reed et al. 2015; WASP-19, $\rho_{\text{spot}} = 0.78$: Tregloan-Reed et al. 2013). This indicates that ρ_{spot} of a typical starspot anomaly lying within the photosphere of a M dwarf star, observed in the T -passband, is below the critical threshold to be detected by ground-based telescopes and implies that starspot anomalies should be detected in TESS transit light curves.

2.2. Parameter impact on the shape of a starspot anomaly

Before we begin simulating starspot anomalies in transit light curves, we need to examine the parameters which directly or indirectly influence the size (amplitude) and shape (duration) of the anomaly. The parameters can be divided into four groups.

- Starspot parameters.
- Stellar and planetary parameters.
- Orbital parameters.
- Observing constraints

The first group of parameters belong to the starspot itself θ , ϕ , r_{spot} and ρ_{spot} (or T_{spot}). The amplitude of a starspot anomaly is directly proportional to ρ_{spot} and the surface area of the starspot (Tregloan-Reed et al. 2013). As ρ_{spot} decreases (i.e., the starspot darkens / cools), r_{spot} must reduce, to maintain the amplitude of the starspot anomaly. In essence, a small starspot, will need a large ratio between T_{spot} and T_{eff} , to be detected (see Eq. 2). The location of the starspot, θ and ϕ have an indirect effect on the amplitude and duration of the anomaly. When the position of the starspot approaches the limb of the star, there is a reduction in the 2D projection of the spot's surface area, due to foreshortening along the radial vector (the vector between the centres of the stellar disc and starspot). Hence, reducing the amplitude of the starspot anomaly. As the radial vector, rotates (by altering the Azimuth angle) to being parallel with the transit cord, the anomaly's duration will be reduced too.

The next group of parameters is related to the host star; T_{eff} , R_* and the planet; R_p . It was shown in both Section 2.1 and Eq. 2 how T_{eff} directly alters ρ_{spot} thereby, indirectly influencing the amplitude of the anomaly. The amplitude of a starspot anomaly is also directly proportional to k , the ratio between R_p and R_* (Tregloan-Reed et al. 2013). If k is too small in relation to the noise then the change in flux due to the planet occulting the starspot, will not be detectable over the noise in the light curve.

The orbital parameters i , a and P all indirectly impact the amplitude and duration of the starspot anomaly. i controls the impact parameter (b) and therefore, i controls the stellar latitude at which the transit cord will cross. Because occulted starspots must lie on the transit chord to be observed then as i decreases, the position of the starspot will move towards the stellar pole (i.e., the limb of the stellar disc). By doing so, the 2D projection of the starspot's surface area will decrease due to foreshortening. b is also controlled by a combined with the orbital eccentricity (e) and the argument of periastron (ω) (e.g., Winn 2010):

$$b = \frac{a \cos i}{R_*} \left(\frac{1 - e^2}{1 + e \sin \omega} \right). \quad (3)$$

Because P is related to a via Kepler's third law and directly controls the transit duration (e.g., Winn 2010), it becomes apparent how a and P can both directly control the duration and indirectly influence the amplitude of the starspot anomaly.

The final group consists of just two parameters ν and the observing cadence. In Section 2.1 it was shown how ν alters the amplitude of the starspot anomaly. Where the amplitude

of the starspot anomaly increases towards bluer wavelengths and reduces towards redder wavelengths. The observing cadence though, does not physically affect the size or shape of the starspot anomaly. However, it does alter our perception of the size and shape. When the cadence decreases (from high to low cadence), the number of data points that describe the starspot anomaly will decrease, altering our perception of the anomaly's true shape. This will increase the uncertainty in the anomaly's duration, and so, increase the uncertainty in the measured parameters which influences the duration of the starspot anomaly.

Because these simulations are based on TESS transit light curves, the observational cadence is fixed at 2 min (Stassun et al. 2018) and ν is fixed at 600 nm, 785 nm & 1000 nm (Sullivan et al. 2015). Consequently both the cadence and ν are considered as constraints and are used in the simulations, at fixed values.

2.3. Simulating starspots in TESS transit light curves

The primary goal of this work is to find the detection limits of starspot anomalies appearing within TESS exoplanet light curves. TESS was developed to find small planets ($< 6 R_{\oplus}$) orbiting local K and M dwarf stars (Ricker et al. 2009). Due to this, the host star and planetary properties used in these simulations were based on the selections used by Sullivan et al. (2015, 2017), covering K & M late-type stars with small planets, $< 6 R_{\oplus}$.

When predicting the planetary yields of TESS Sullivan et al. (2015) calculated that TESS will have a photometric sensitivity of 200 ppm for an I_C 10th magnitude star. Because of this, the light curves generated by PRISM had added Gaussian noise: 60 ± 3 ppm⁴, 100 ± 5 ppm, 150 ± 7.5 ppm and 200 ± 10 ppm. By doing so, allows us to simulate the photometric sensitivity of light curves for host stars brighter than $I_C = 10$ (after undergoing the TESS data processing pipeline and known systematics removal, see Jenkins et al. 2016).

With the TESS observations being performed in the T -passband (600 nm–1000 nm; Sullivan et al. 2015) the simulations were run at three wavelengths: 600 nm, 785 nm and 1000 nm. These wavelengths were selected to give a good average approximation to the T -passband (785 nm) and to obtain results at the bluest (600 nm) and reddest (1000 nm) edge of the T -passband spectral response, and so, produce the largest and smallest amplitudes for the starspot anomalies.

Examining the range of parameters described in Section 2.2 it becomes apparent that the parameter space which controls the amplitude and duration of a starspot anomaly, is large and complex due to multiple degeneracies between the parameters (e.g., $r_{\text{spot}} \leftrightarrow \rho_{\text{spot}}$, $\phi \leftrightarrow i$, $P \leftrightarrow a$ and $\phi \leftrightarrow P$). However, for this work we are only interested in the detection limits of starspot anomalies found within TESS light curves (i.e., smallest r_{spot} for a given scenario). Therefore we can streamline the parameter space by using a mixture of predetermined key parameter values / scenarios (e.g., setting R_* and T_{eff} for typical K & M dwarf stars) and search for the smallest detectable r_{spot} .

In the simulations the position of the starspot was set at the centre of the stellar disc, therefore, minimising the effect from foreshortening. As discussed in Section 2.2 foreshortening reduces the amplitude of the starspot anomaly. Therefore, due to the geometric nature of spherical foreshortening, the smallest detectable r_{spot} will be for starspots lying at the centre of the stellar disc. This is because when the starspot moves closer to the limb,

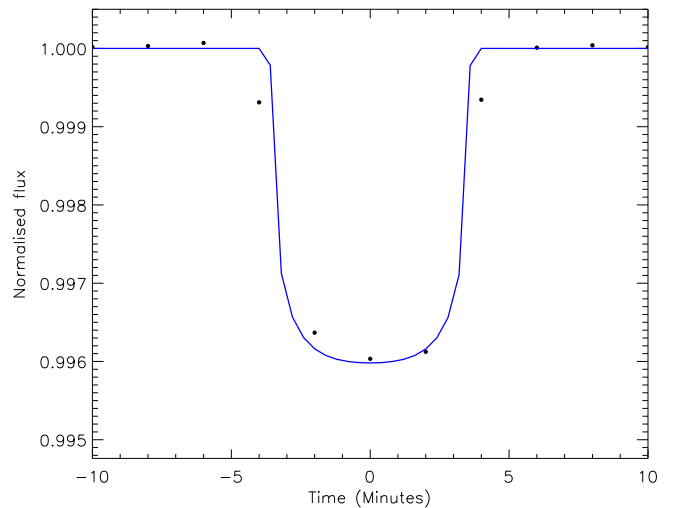


Fig. 1. Simulated two minute cadence TESS light curve, of a $1 R_{\oplus}$ planet orbiting an M4V dwarf star with $P = 12$ d and an rms scatter of 104 ppm (generated by PRISM). The transit duration is approximately eight minutes and only three data points lie within the transit.

r_{spot} needs to increase, so to maintain the same two dimensional projected surface area of the starspot. Because we want to detect the smallest starspot for a given set of circumstances. Placing the starspot at the centre of the stellar disc, will achieve this.

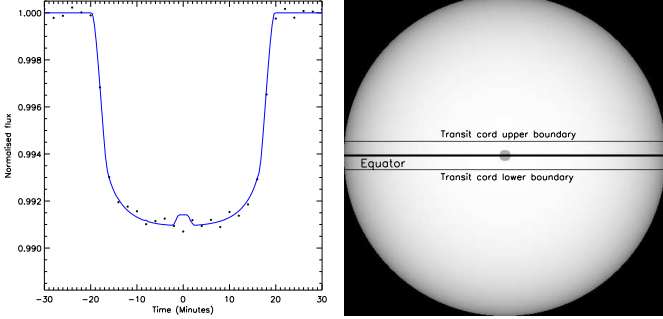
To determine TESS planetary yields Sullivan et al. (2015, 2017) used an M4V dwarf with $T_{\text{eff}} = 3200$ K, a radius of $R_* = 0.155 R_{\odot}$, solar metallicity and at 1 Gyr (in keeping with the Dartmouth Stellar Evolution Database Dotter et al. 2008). The T_{eff} was selected because M dwarfs cooler than 3200 K, will be too faint for planetary transit detection in the T passband (Sullivan et al. 2015). For this work it was therefore natural to start with an M4V dwarf star. The smaller value for R_* and by association, larger k , meant that a $1 R_{\oplus}$ radius could be used in the M4V dwarf simulations. The planetary radii used, ranged from $1-3 R_{\oplus}$ in $0.25 R_{\oplus}$ increments. An upper limit of $3 R_{\oplus}$ was used due to the rare occurrence of close in (< 50 d), large ($> 3 R_{\oplus}$) planets orbiting M dwarf stars, determined from population studies using Kepler and K2 data (Dressing & Charbonneau 2013, 2015; Morton & Swift 2014). Though the recent discovery of NGTS-1 b: an $\approx 15 R_{\oplus}$ hot-Jupiter transiting an M0.5 dwarf star with a 2.65 d orbital period (Bayliss et al. 2018), along with two previously known close in large planets transiting M dwarfs (Kepler-45 b; Johnson et al. 2012; HATS-6 b; Hartman et al. 2015) appears to be lifting this limit.

A key objective of TESS is to find suitable planets for further study within the habitable zone of the host star. For a planet orbiting an M4V dwarf star with a relative insolation (S/S_{\oplus}) set at the inner ($S/S_{\oplus} = 1.0$), mean ($S/S_{\oplus} = 0.6$) and outer edge ($S/S_{\oplus} = 0.2$) of the habitable zone (Kopparapu et al. 2013) will have an orbital period between 12 and 40 days (Eq. 13 Sullivan et al. 2015). The difficulty in detecting starspot anomalies at these orbital periods is that the transit duration, is less than 10 minutes (see Fig. 1). This results in the duration of a starspot anomaly being less than a minute, which is not favourable when using two minute cadence data. Unlike transit detections, which can use phase-folded light curves to increase the number of data points within the transit, and so, aid in the transit detection, a starspot anomaly can generally only be detected using a single transit, due to the rotation of the host star smearing the different positions of the starspot anomaly when viewing multiple phase-

⁴ Mission specified noise floor at 60 ppm hr^{1/2} (see Sullivan et al. 2015)

Table 1. Calculated values of a for each value of P , for the three simulated host stars.

M4V		M1V		K5V	
P (d)	a (AU)	P (d)	a (AU)	P (d)	a (AU)
1.0	0.0091	2.0	0.0242	2.0	0.0269
2.0	0.0144	3.0	0.0317	4.0	0.0427
3.0	0.0189	4.0	0.0383	6.0	0.0560

**Fig. 2.** Example light curve (left) and stellar disc (right) generated by PRISM. Light curve: The solid line represents the noise-free synthetic light curve containing the starspot anomaly, while the filled circles represent the “spot-free” synthetic light curve (see Section 3) with added Gaussian noise. Stellar disc: The central solid line represents the stellar equator (assuming orbital alignment) and the upper and lower solid lines represent the upper and lower boundaries of the transit cord. These were generated with a $1.5R_{\oplus}$ super-Earth planet transiting a 3200 K, $0.155R_{\odot}$ M4V dwarf star with $i = 90.0^{\circ}$ and $P = 1$ d. The starspot properties are: $\theta = 0^{\circ}$, $\phi = 90^{\circ}$, $r_{\text{spot}} = 0.035R_{*}$ and $T_{\text{spot}} = 3000$ K. The observational wavelength and the rms scatter for the simulated data were set at 785 nm and 150 ± 7.5 ppm respectively.

folded light curves. Due to this, the orbital period in the M4V dwarf simulations was set at 1, 2 and 3 days, to allow sufficient sampling in the single light curves to detect a starspot anomaly. It should be stated though, that a subset of TESS data will be made available with a cadence of less than two minutes (20 s) for the asteroseismology community (Ricker et al. 2015).

Kepler’s third law was used to calculate a from P using a stellar mass, $M_{*} = 0.1 M_{\odot}$ and are given in Table 1. The stellar mass was determined using $R_{*} = 0.155 R_{\odot}$ combined with Eq. 10 (second order polynomial) from Boyajian et al. (2012), derived from interferometric measurements of M & K dwarfs. We then calculated $\log g = 5.06$ for the M4V dwarf and combined with $T_{\text{eff}} = 3200$ K, determined the quadratic limb darkening coefficients, u_1 & u_2 (Table 2) using grids developed by Claret (2017) using stellar atmosphere models and are designed for use in the TESS passband.

Barnes et al. (2015) looked at starspot distributions of two fully convective M dwarfs, M4.5V: GJ 791.2 A and M9V: LP 944-20 and found starspot temperatures around 200 K to 300 K cooler than the surrounding photosphere. In-line with this, we select four equidistant starspot temperatures 3000 K, 3050 K, 3100 K and 3150 K for the 3200 K M4V dwarf simulations.

1296 different scenarios were used for the M4V dwarf star simulations. Each scenario was derived from alternating the nine R_p , three orbital periods, three observational wavelengths (600 nm, 785 nm and 1000 nm), four starspot temperatures and four noise levels (60 ppm, 100 ppm, 150 ppm and 200 ppm). r_{spot} was then varied to find the detection limit for each of the 1296 scenarios. Fig. 2 shows an example light curve and stellar disc from PRISM for one of the simulations.

Table 2. Extrapolated values of R_{*} and M_{*} using T_{eff} from polynomials derived from interferometric measurements of M & K dwarf stars (Eq. 8 & 10 Boyajian et al. 2012), for the three simulated host stars combined with the calculated $\log g$ and u_1 & u_2 for the quadratic limb darkening law from Claret (2017).

Spectral Type	T_{eff} (K)	R_{*} (R_{\odot})	M_{*} (M_{\odot})	$\log g$ (cgs)	u_1	u_2
M4V	3200	0.155	0.10	5.06	0.1533	0.4776
M1V	3700	0.493	0.52	4.77	0.1737	0.4118
K5V	4100	0.623	0.65	4.66	0.3955	0.2618

Due to the small radius ($R_{*} = 0.155 R_{\odot}$) of the initial host star, the second host star used in the simulations was a larger M1V dwarf star, with $T_{\text{eff}} = 3700$ K (Table 1 Sullivan et al. 2015). This allowed the simulations to examine the detection limit of starspot anomalies at the two ends of the range of R_{*} and T_{eff} of M dwarfs, observed by TESS. The R_{*} and M_{*} of the M1V dwarf were extrapolated using the polynomials derived from interferometric measurements of M & K dwarfs (Eq. 8 & 10 Boyajian et al. 2012) using $T_{\text{eff}} = 3700$ K. The results⁵ are given in Table 2 along with the extrapolated properties of the M4V and K5V dwarf host stars. We employ the same procedure that was used for the M4V dwarf in determining u_1 and u_2 from Claret (2017) with the results reported in Table 2.

Due to a threefold increase in the stellar radius, the planetary radii used in the M1V simulations ranged from $2-4R_{\oplus}$ in $0.25R_{\oplus}$ increments. Three orbital periods were selected at 2, 3 & 4 days and the corresponding values for a were calculated using Kepler’s third law using a stellar mass of $0.52 M_{\odot}$ (see Table 2) and are given in Table 1. Using an $T_{\text{eff}} = 3700$ K for the M1V dwarf star, four equidistant starspot temperatures were selected: 3400 K, 3475 K, 3550 K and 3625 K, giving a further 1296 different scenarios (Using the same three observational wavelengths and four noise levels that were used in the M4V dwarf simulations) using an M1V dwarf host star. The same procedure that was used in the M4V simulations was used for the M1V simulations. In that for each of the 1296 scenarios, r_{spot} was varied to find the detection limit in each scenario.

For the third host star, a K5V dwarf star was selected. Using an $T_{\text{eff}} = 4100$ K (Table 1 Sullivan et al. 2015), the R_{*} and M_{*} was extrapolated from the two polynomials presented by Boyajian et al. (2012) and are given in Table 2. We determine u_1 and u_2 from Claret (2017), for the K5V dwarf and are given in Table 2.

Because of the larger R_{*} the K5V simulations probed the detection limits of starspot anomalies for larger planets, $3-7R_{\oplus}$ (Sub-Neptune to sub-Saturn class planets) in $0.5R_{\oplus}$ increments. Due to the larger R_{*} and R_p the three values of P were selected at 2, 4 & 6 days with the corresponding values for a calculated using Kepler’s third law using a stellar mass of $0.65 M_{\odot}$ (see Table 2) and are given in Table 1. With $T_{\text{eff}} = 4100$ K four temperatures were selected for the starspot 3700 K, 3800 K, 3900 K and 4000 K. Combined with the three observational wavelengths and four noise levels meant that a further 1296 scenarios were generated using an K5V dwarf host star.

⁵ We ignore the coefficient uncertainties in the polynomials presented by Boyajian et al. (2012) as we are generating hypothetical host stars, whose physical properties are consistent with the physical properties of observed stars of the same spectral type.

3. Simulation Results

For all 3888 different scenarios a total of 20573 simulated transits were generated. All 20573 simulated transit light curves will be made available at the CDS⁶. The number of simulated transits per scenario was dependent on the detection of r_{spot} and ranged from 2 - 40 simulations per scenario, where r_{spot} started at $0.0087R_*$ and was increased in $0.0087R_*$ steps up to $0.35R_*$. The simulations were stopped when the starspot anomaly was deemed detectable. The starspot anomaly was considered “detected” in the simulated transits, if the characteristic “blip” was visible in the simulated light curve (e.g., Fig. 2). This was accomplished by comparing the amplitude of the anomaly to the photometric precision (rms scatter) of the data. The amplitude of the starspot anomaly was measured by creating two transit light curves. The first had the centre of the starspot within the transit cord while the second light curve had the starspot latitude shifted so that it was no longer within the transit cord. Because both occulted and non-occulted starspots affect the shape of the light curve (Silva-Válho 2010) and in particular the transit depth (Nikolov et al. 2013) it was important that the stellar disc of the “spot-free” light curve model still contained a starspot of equal properties. To reduce the impact from foreshortening, the starspot was positioned so that only a gap of one pixel separated the starspot and transit cord boundaries. We compared the resulting light curves to determine the amount of systematic error the approximation would generate and found a mean divergence of ≈ 1 ppm, 60 times smaller than the TESS mission specified noise floor. Therefore, we conclude that this approximation is suitable for this work.

The light curve plots produced in this work show two synthetic light curves represented by a solid line and filled circles. The light curves represented by a solid line are the synthetic light curves containing the starspot anomaly and are without added noise. The light curves represented by filled circles are the synthetic light curves of the “spot-free” model and have added Gaussian noise. By comparing the two synthetic light curves it is possible to determine if the amplitude of the starspot anomaly is larger than the rms scatter.

To determine the most efficient set of detection conditions, tests were performed on the synthetic data. After the addition of noise to the synthetic light curve, PRISM was fitted to the synthetic light curve in an attempt to recover the starspot parameters. The amplitude of the starspot anomaly was determined by the data points which described the starspot anomaly and the mean change in flux was calculated. The mean change in flux was then divided by the rms scatter of the light curve to give the amplitude of the starspot anomaly in units of rms (σ). Different amplitudes were considered from $1\text{-}\sigma$ to $3\text{-}\sigma$. In all cases where the amplitude was greater than $2.0\text{-}\sigma$, the best fitting starspot parameters of the synthetic light curves were close to the original values and agreed within their $1\text{-}\sigma$ parameter uncertainties. However, when the amplitude of the starspot anomaly was between $1.5\text{-}\sigma$ and $2\text{-}\sigma$ the $1\text{-}\sigma$ uncertainty in the starspot parameters was non-physical. For example in one test the starspot radius was found to be $0.047R_* \pm 1.700R_*$ indicating that the starspot covered the entire visible hemisphere of the stellar disc, and in another test the latitude of the starspot was found to be $0.17^\circ \pm 97.39^\circ$, which indicated that a spot-free solution (i.e., the starspot was no longer on the transit cord) was an acceptable solution. These tests showed that when the amplitude of the starspot anomaly was between $1.5\text{-}\sigma$ and $2\text{-}\sigma$ the anomaly could be detected but

it was not possible to constrain the starspot parameters, and so, confirm the presence of a starspot. Therefore, the optimal cut-off point for the amplitude of the starspot anomaly was set at the $2\text{-}\sigma$ limit to differentiate between a detection and non-detection.

3.1. M4V dwarf host star results

A total of 6870 simulations were conducted for the 1296 scenarios using an M4V dwarf host star and the results are presented in Table A.1. It was found that the starspot detection limit in TESS transit light curves of an M4V dwarf host star was $r_{\text{spot}} = 0.045R_* \pm 0.016R_*$ (4900 ± 1700 km), where the uncertainty is the $1\text{-}\sigma$ standard deviation from the 1296 scenarios of the M4V host star simulations. The smallest r_{spot} detected in the M4V simulations (under optimal parameter conditions) was $r_{\text{spot}} = 0.017R_*$ or 1900 km (see Fig. 3) and was detected in 7 of the 1296 scenarios (0.5 %).

It was found that for three scenarios, it was not possible to resolve the starspot size (see Fig. 4). These scenarios involved a 3150 K starspot with a photometric precision of 200 ppm, observed at 1000 nm and with an $1R_\oplus$ transiting planet. When examining the stellar disc output for the $0.093R_*$ starspot in Fig. 4, the area of the 2D projection of the starspot is larger than the planetary disc. Therefore, increasing r_{spot} further, would no longer increase the amplitude of the starspot anomaly, because it would not affect the amount of flux blocked by the planet. However, it will increase the duration, due to the fact, that the planet will spend longer occulting the starspot. This can be seen when examining the three simulated light curves in Fig. 4. Therefore, for these scenarios, the amplitude of the starspot anomaly never became larger than the rms scatter of the synthetic data.

Hence, the simulations show that it is not possible to observe a 3150 K starspot on the surface of a 3200 K M4V dwarf, using a $1.0R_\oplus$ Earth-sized planet, when observed at the reddest edge of the T passband (i.e., 1000 nm) with an rms scatter of 200 ppm. However, by either increasing the planetary radius ($+0.25R_\oplus$), reducing the rms scatter (-50 ppm) or shifting to a bluer wavelength, it would be possible to detect these starspots down to $0.035R_*$ (3800 km) (see Table A.1).

3.2. M1V dwarf host star results

A total of 7769 simulations were conducted for the 1296 scenarios using an M1V dwarf host star and the results are presented in Table A.2. It was found that the starspot detection limit in TESS transit light curves of an M1V dwarf host star was $r_{\text{spot}} = 0.040R_* \pm 0.017R_*$ (13800 ± 6000 km). The smallest r_{spot} detected in the M1V simulations (under optimal parameter conditions) was $r_{\text{spot}} = 0.017R_*$ or 6000 km (see Fig. 5) and was detected in 85 of the 1296 scenarios (6.6 %).

To allow for a direct comparison between the starspots on the M1V and M4V dwarf stars requires the M1V dwarf star, r_{spot} to be multiplied by $\left(\frac{R_{\text{M1V}}}{R_{\text{M4V}}}\right) \approx 3.2$. From this it can be seen that while the smallest starspot detected in the M1V dwarf simulations had $r_{\text{spot}} = 0.017R_*$, this is the equivalent to $r_{\text{spot}} \approx 0.056R_*$ for a M4V dwarf star.

Similar to the M4V host star results, the M1V host star results show that it is not possible to detect the hottest starspots when small planets (e.g., $< 2.75R_\oplus$) are transiting the star, if the photometric precision is > 100 ppm.

⁶ <http://vizier.u-strasbg.fr/>

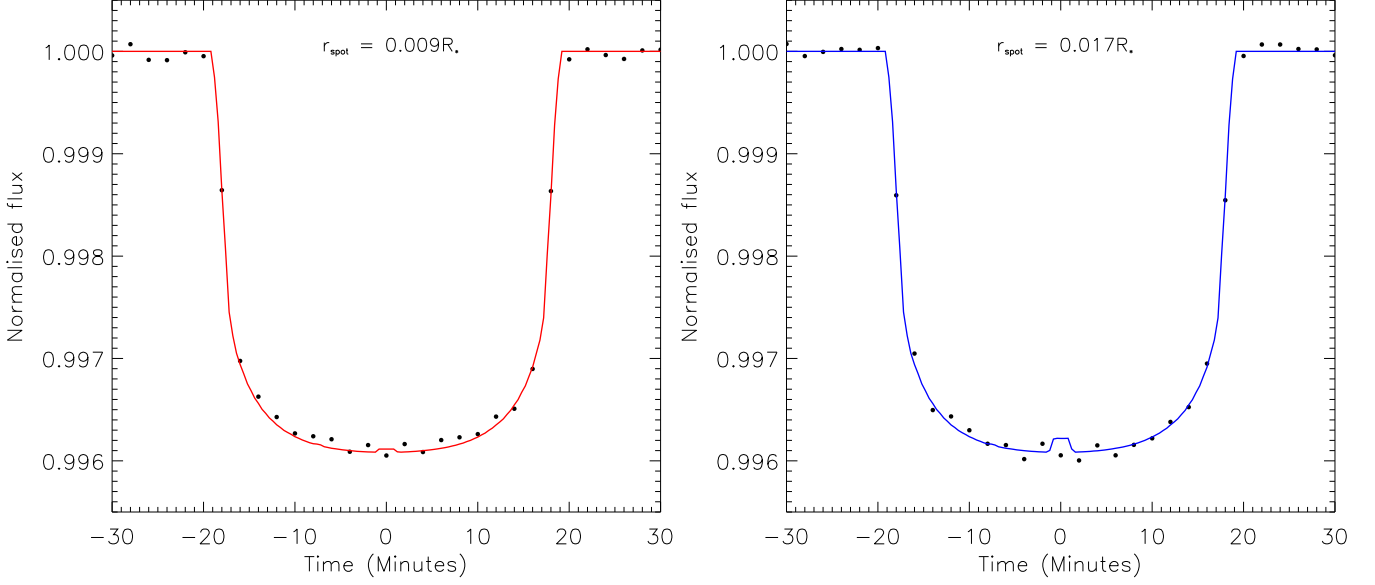


Fig. 3. Two simulated transit light curves generated by PRISM. These were both generated using a $1.0R_{\oplus}$ Earth-sized planet transiting a 3200 K, $0.155R_{\odot}$ M4V dwarf star with $i = 90.0^{\circ}$ and $P = 1$ d. The starspot properties are: $\theta = 0^{\circ}$, $\phi = 90^{\circ}$, $r_{\text{spot}} = 0.009R_*$ (left), $r_{\text{spot}} = 0.017R_*$ (right) and $T_{\text{spot}} = 3000$ K. The observational wavelength and the rms scatter for the simulated transits were set at 600 nm and 60 ppm respectively. The starspot anomaly becomes visible over the simulated noise when r_{spot} is increased from $0.009R_*$ to $0.017R_*$. The solid lines represents the noise-free synthetic light curves containing the starspot anomaly, while, the filled circles represent the “spot-free” synthetic light curves (see Section 3) with added Gaussian noise.

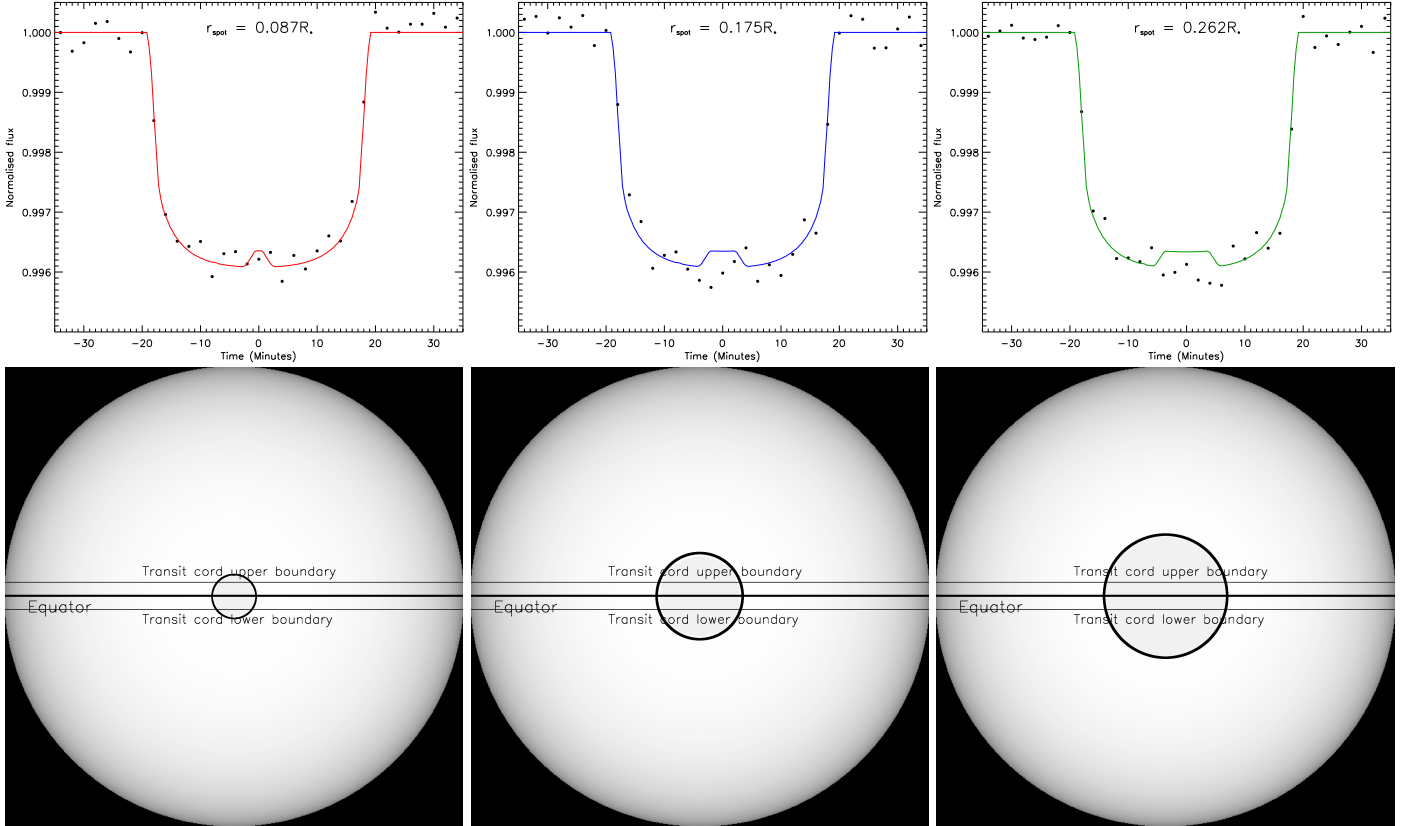


Fig. 4. Three simulated transit light curves (top panels) and stellar disc outputs (bottom panels), generated by PRISM. Light curves: The solid lines represents the noise-free synthetic light curves containing the starspot anomaly, while, the filled circles represent the “spot-free” synthetic light curves (see Section 3) with added Gaussian noise. Stellar discs: The central solid lines represents the stellar equator (assuming orbital alignment) and the upper and lower solid lines represent the upper and lower boundaries of the transit cords. Due to the high ρ_{spot} , the starspot boundary has been highlighted with a black circular boarder. The observational wavelength and the rms scatter for the simulated transits were set at 1000 nm and 200 ppm respectively. These were generated using a $1.0R_{\oplus}$ Earth-sized planet transiting a 3200 K, $0.155R_{\odot}$ M4V dwarf star with $i = 90.0^{\circ}$ and $P = 1$ d. The starspot properties were set at: $\theta = 0^{\circ}$, $\phi = 90^{\circ}$ and $T_{\text{spot}} = 3150$ K ($\rho_{\text{spot}} = 0.93$). The left panels have $r_{\text{spot}} = 0.087R_*$, the middle panels have $r_{\text{spot}} = 0.175R_*$ and the right panels have $r_{\text{spot}} = 0.262R_*$.

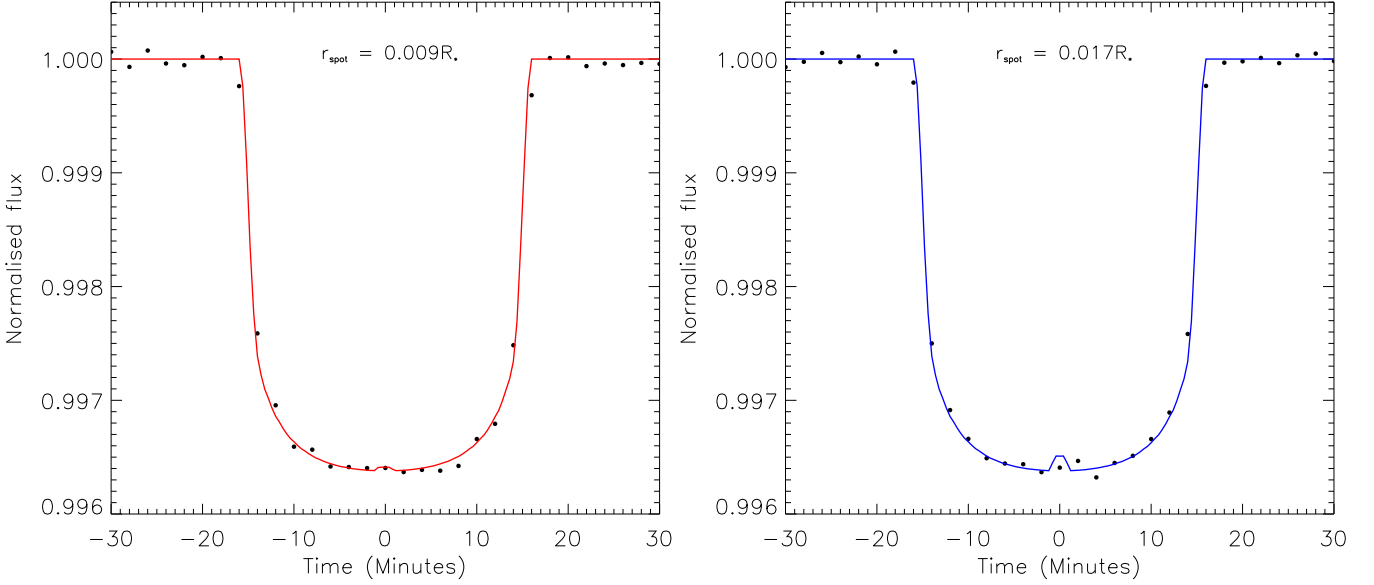


Fig. 5. Two simulated transit light curves generated by PRISM. These were both generated using a $2.75 R_{\oplus}$ sub-Neptune planet transiting a 3700 K, $0.493 R_{\odot}$ M1V dwarf star with $i = 90.0^{\circ}$ and $P = 3$ d. The starspot properties are: $\theta = 0^{\circ}$, $\phi = 90^{\circ}$, $r_{\text{spot}} = 0.009 R_*$ (left), $r_{\text{spot}} = 0.017 R_*$ (right) and $T_{\text{spot}} = 3400$ K. The observational wavelength and the rms scatter for the simulated transits were set at 785 nm and 60 ppm respectively. The starspot anomaly becomes visible over the simulated noise when r_{spot} is increased from $0.009 R_*$ to $0.017 R_*$. The solid lines represent the noise-free synthetic light curves containing the starspot anomaly, while, the filled circles represent the “spot-free” synthetic light curves (see Section 3) with added Gaussian noise.

3.3. K5V dwarf host star results

A total of 5934 simulations were conducted for the 1296 scenarios using a K5V dwarf host star and the results are presented in Table A.3. It was found that the starspot detection limit in TESS transit light curves of a K5V dwarf host star was $r_{\text{spot}} = 0.038 R_* \pm 0.016 R_*$ (15900 ± 6800 km). The smallest r_{spot} detected in the K5V simulations (under optimal parameter conditions) was $r_{\text{spot}} = 0.017 R_*$ or 7600 km (see Fig. 6) and was detected in 102 of the 1296 scenarios (7.9 %).

We use the same process described in Section 3.2 to compare the starspot sizes on the K5V and M4V dwarf stars. We find that for the K5V dwarf star, r_{spot} should be multiplied by $\left(\frac{0.623}{0.155}\right) \approx 4.0$. The smallest starspot detections for the K5V host star simulations were when $r_{\text{spot}} = 0.017 R_*$, which if the starspots were on a M4V dwarf instead, would equate to a detection with $r_{\text{spot}} \approx 0.07 R_*$.

It was found that for only 15 (1.2 %) scenarios it was not possible to resolve the starspot. These scenarios followed the same pattern as found with the previous host stars. The scenarios involving a high temperature starspot, small planet and observed at redder wavelengths with low photometric precision, tended to prevent the detection of the starspot.

3.4. Expected trends

By examining the results from the 20573 simulated transits (see Tables A.1, A.2, A.3), known trends (described in Section 2.2) in the starspot detection limits are seen.

The simulations confirmed that by increasing the photometric precision (decrease in noise) in the observations, allowed smaller starspots to be detected (e.g., Fig. 7). The simulations also, confirm that the starspot detection limit is dependent on T_{spot} , the observational wavelength and the orbital period (e.g., Fig. 8). It is easier to detect a small cool starspot than a small hot

starspot (top row Fig. 8). Likewise, a shorter orbital period allows the detection of smaller starspots (bottom row Fig. 8). This is due to a longer transit duration and by association, a longer starspot anomaly duration. Thereby increasing the number of data points describing both the transit and the starspot anomaly, due to the fixed 2 min cadence of TESS data.

The simulations help support the predicted / known trends given in Section 2.2 and highlights which parameters the detection limit is strongly or weakly, dependent on. Examining Fig. 8, it can be seen that by doubling the orbital period (P), the minimum detected r_{spot} increases by 20 %, while shifting the observed wavelength from 600 nm to 1000 nm, the minimum detected r_{spot} increases by 50 %. However increasing T_{spot} by 100 K increases the minimum detected r_{spot} by 67 %⁷, indicating that the detection limit is primarily influenced by T_{spot} and λ_{obs} – which is expected – due to the amplitude of a starspot anomaly being directly proportional to ρ_{spot} (see Tregloan-Reed et al. 2013), which in turn is proportional to T_{spot} and λ_{obs} (see Eq. 2).

The amplitude of the starspot anomaly is proportional to $\left(\frac{r_{\text{spot}}}{R_p}\right)^2$ when $r_{\text{spot}} \leq R_p$. Therefore, smaller planets can detect smaller starspots. The results from the simulations agree with this when dealing with cool starspots. However, the simulations depict a different trend when dealing with the hotter starspots, in that, larger planets are able to detect smaller starspots. For example in Table A.1 we can see that a $1.25 R_{\oplus}$ planet transiting a 3200 K, $0.155 R_{\odot}$ M4V dwarf star with $i = 90.0^{\circ}$, $P = 2$ d, $\lambda_{\text{obs}} = 785$ nm and $T_{\text{spot}} = 3150$ K, with rms scatter 150 ± 7.5 ppm, the smallest detected r_{spot} is $r_{\text{spot}} = 0.070 R_*$. While for a $1.5 R_{\oplus}$ and $1.75 R_{\oplus}$ planet the smallest detected r_{spot} becomes $r_{\text{spot}} = 0.061 R_*$ and $r_{\text{spot}} = 0.052 R_*$ respectively.

⁷ For a 3200 K M4V dwarf star, observed at 600 nm.

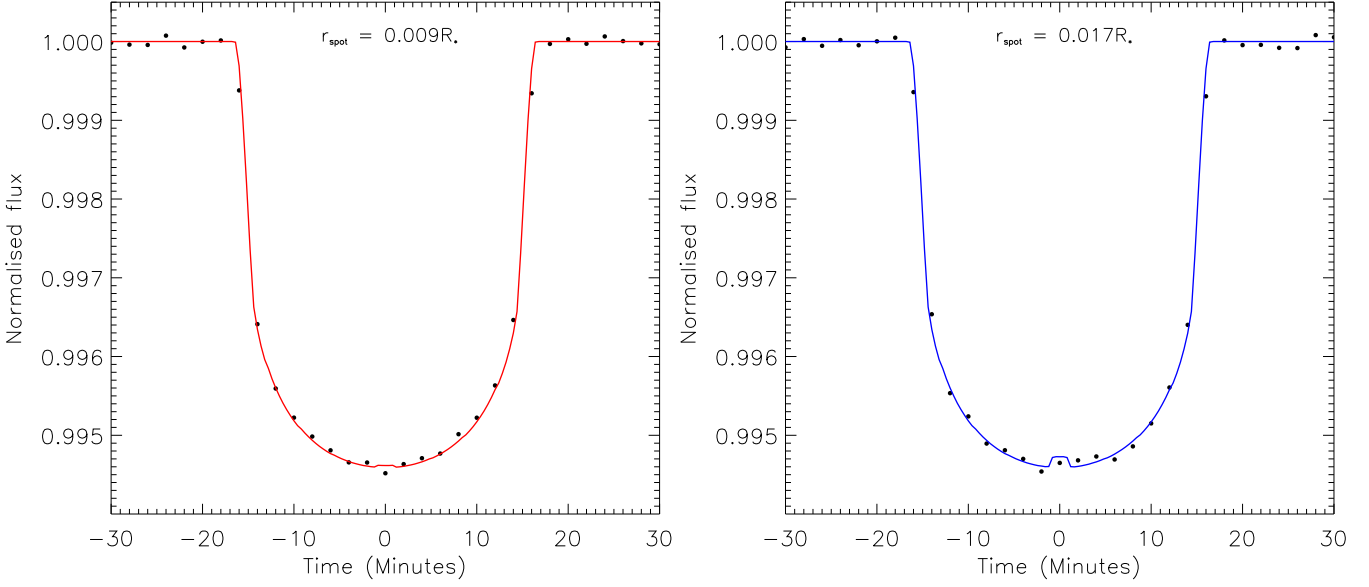


Fig. 6. Two simulated transit light curves generated by PRISM. These were both generated using a $4.5 R_{\oplus}$ Neptune-sized planet transiting a 4100 K, $0.623 R_{\odot}$ K5V dwarf star with $i = 90.0^{\circ}$ and $P = 4$ d. The starspot properties are: $\theta = 0^{\circ}$, $\phi = 90^{\circ}$, $r_{\text{spot}} = 0.009 R_*$ (red), $r_{\text{spot}} = 0.017 R_*$ (blue) and $T_{\text{spot}} = 3700$ K. The observational wavelength and the rms scatter for the simulated transits were set at 785 nm and 60 ppm respectively. The starspot anomaly becomes visible over the simulated noise when r_{spot} is increased from $0.009 R_*$ to $0.017 R_*$. The solid lines represent the noise-free synthetic light curves containing the starspot anomaly, while the filled circles represent the “spot-free” synthetic light curves (see Section 3) with added Gaussian noise.

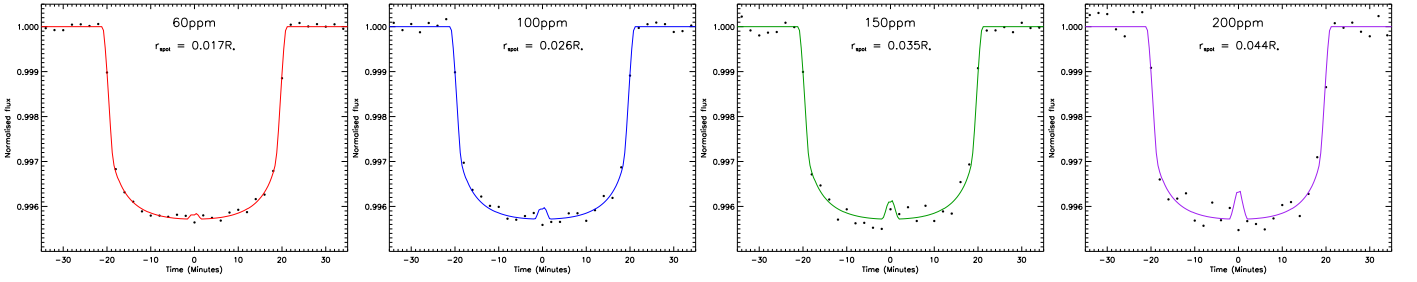


Fig. 7. Four simulated transit light curves, generated by PRISM. The observational wavelength of the simulated transits was 785 nm. These were generated using a $3.0 R_{\oplus}$ sub-Neptune planet transiting a 3700 K, $0.493 R_{\odot}$ M1V dwarf star with $i = 90.0^{\circ}$ and $P = 2$ d. The starspot properties were set at: $\theta = 0^{\circ}$, $\phi = 90^{\circ}$ and $T_{\text{spot}} = 3475$ K. The rms scatter of the light curves from left to right are 60 ppm, 100 ppm, 150 ppm and 200 ppm. Each light curve shows the smallest detectable starspot size for the scenarios, $0.017 R_*$ (red), $0.026 R_*$ (blue), $0.035 R_*$ (green) and $0.044 R_*$ (purple), which increases with increasing noise. The solid lines represent the noise-free synthetic light curves containing the starspot anomaly, while the filled circles represent the “spot-free” synthetic light curves (see Section 3) with added Gaussian noise.

3.5. Unexpected trend

Table 3 shows the comparison between R_p and the statistical mean of the starspot detection limit (\bar{r}_{spot}), including its $1-\sigma$ uncertainty. At first glance, Table 3 seems to be in contradiction with the statement “small planets are needed to detect small starspots”. However, looking at the top row of Table 3, we see that when the $1-\sigma$ uncertainty in \bar{r}_{spot} is taken into account, we see that the smallest planet (e.g., $R_p = 1 R_{\oplus}$) can detect the smallest starspot (e.g., $\bar{r}_{\text{spot}} = 0.018 R_*$). The results in Table 3 also indicate that the range of values for \bar{r}_{spot} , reduce with increasing R_p .

When examining tables A.1, A.2, A.3, we can see an unexpected trend emerging: starspots which are small and hot can be detected by large planets, however, they can’t be detected by smaller planets. This unexpected and counter-intuitive trend, however, is a manifestation, from using a fixed cadence combined with the methodology used to detect starspot anomalies in transit light curves.

Increasing R_p will not only increase the transit duration, it will also increase the duration of the starspot anomaly. This is because a larger planetary disc will spend longer occulting the starspot. For a fixed cadence (2 mins for TESS) this will equate to an increase in the number of data points which will describe the starspot anomaly. As mentioned in Section 3 the mean flux of the data points within the starspot anomaly was used to determine if the starspot had been detected. This is in principle the same method used to detect starspot anomalies in observed light curves. In the case when a single data point describes the apex of a starspot anomaly (i.e., the 2D projection of r_{spot} equals R_p ; Fig. 9) the data points which lie within the ingress and egress of the starspot anomaly will reduce the mean flux. For a starspot anomaly that’s described by multiple data points which form a plateau (i.e., the 2D projection of r_{spot} is either larger or smaller than R_p ; Fig. 10) the mean flux will increase due to the data points lying on the starspot ingress and egress, having a weaker impact. Because of this, a starspot with an apex will require a larger amplitude to be detected. This is correct as a single data

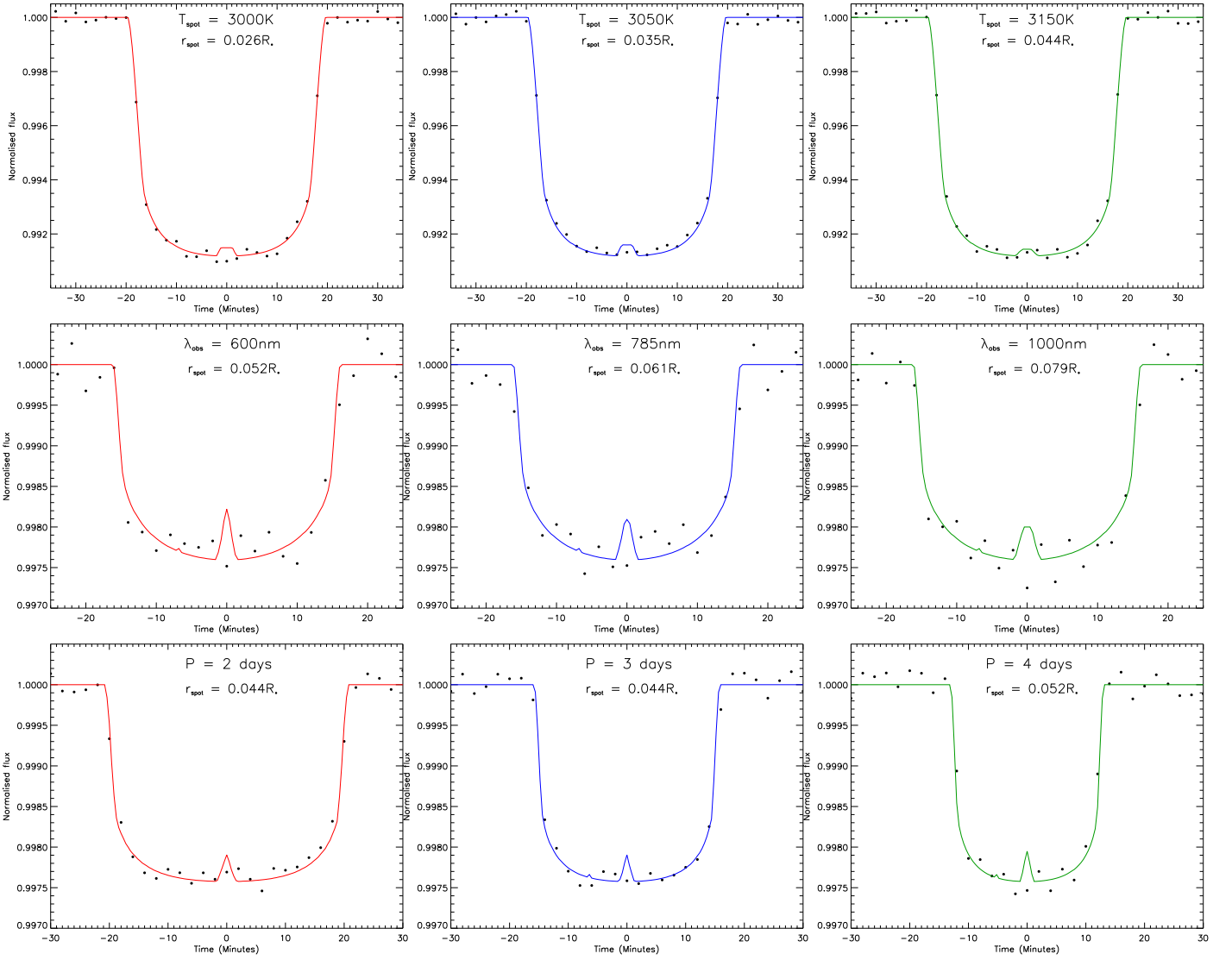


Fig. 8. Nine simulated transit light curves, generated by PRISM, showing the smallest detected starspot for three trends, T_{eff} : top row; λ_{obs} : middle row; P : bottom row. (*Top row*) simulations of a $1.5R_{\oplus}$ super-Earth planet transiting a 3200 K, $0.155R_{\odot}$ M4V dwarf star with $i = 90.0^{\circ}$, $P = 1$ d, $\lambda_{\text{obs}} = 600$ nm and $T_{\text{spot}} = 3000$ K, 3050 K and 3100 K (left to right). With rms scatter 150 ± 7.5 ppm. The smallest detected r_{spot} are: $r_{\text{spot}} = 0.026R_{*}$ (red), $r_{\text{spot}} = 0.035R_{*}$ (blue), $r_{\text{spot}} = 0.044R_{*}$ (green). (*Middle row*) simulations of a $3.0R_{\oplus}$ Neptune size planet transiting a 4100 K, $0.623R_{\odot}$ K5V dwarf star with $i = 90.0^{\circ}$, $P = 4$ d, $T_{\text{spot}} = 3900$ K and $\lambda_{\text{obs}} = 600$ nm, 785 nm and 1000 nm (left to right). With rms scatter 200 ± 10 ppm. The smallest detected r_{spot} values are: $r_{\text{spot}} = 0.052R_{*}$ (red), $r_{\text{spot}} = 0.061R_{*}$ (blue), $r_{\text{spot}} = 0.079R_{*}$ (green). (*Bottom row*) simulations of a $2.25R_{\oplus}$ sub-Neptune planet transiting a 3700 K, $0.493R_{\odot}$ M1V dwarf star with $i = 90.0^{\circ}$, $T_{\text{spot}} = 3550$ K, $\lambda_{\text{obs}} = 1000$ nm and $P = 2$ d, 3 d and 4 d (left to right). With rms scatter 100 ± 5 ppm. The smallest detected r_{spot} are: $r_{\text{spot}} = 0.044R_{*}$ (red), $r_{\text{spot}} = 0.044R_{*}$ (blue), $r_{\text{spot}} = 0.052R_{*}$ (green). The solid lines represents the noise-free synthetic light curves containing the starspot anomaly, while, the filled circles represent the “spot-free” synthetic light curves (see Section 3) with added Gaussian noise.

Table 3. Comparison between R_p and \bar{r}_{spot} for the M4V, M1V and K5V host stars.

M4V		M1V		K5V	
$R_p (R_{\oplus})$	$\bar{r}_{\text{spot}} (R_{*})$	$R_p (R_{\oplus})$	$\bar{r}_{\text{spot}} (R_{*})$	$R_p (R_{\oplus})$	$\bar{r}_{\text{spot}} (R_{*})$
1.00	0.042 ± 0.024	2.00	0.045 ± 0.028	3.0	0.044 ± 0.031
1.25	0.038 ± 0.014	2.25	0.044 ± 0.023	3.5	0.040 ± 0.023
1.50	0.038 ± 0.012	2.50	0.042 ± 0.021	4.0	0.037 ± 0.017
1.75	0.038 ± 0.010	2.75	0.042 ± 0.021	4.5	0.035 ± 0.014
2.00	0.040 ± 0.010	3.00	0.040 ± 0.019	5.0	0.035 ± 0.012
2.25	0.044 ± 0.010	3.25	0.038 ± 0.016	5.5	0.035 ± 0.012
2.50	0.045 ± 0.010	3.50	0.037 ± 0.014	6.0	0.035 ± 0.010
2.75	0.051 ± 0.014	3.75	0.037 ± 0.014	6.5	0.035 ± 0.010
3.00	0.054 ± 0.014	4.00	0.037 ± 0.012	7.0	0.035 ± 0.010

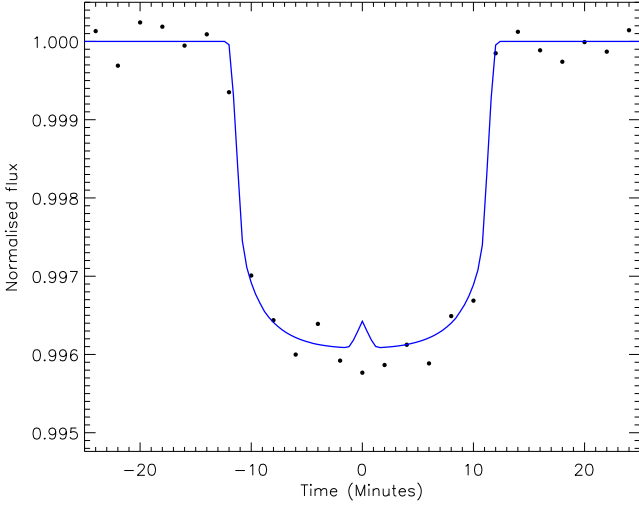


Fig. 9. Example of a single data point describing the apex of a starspot anomaly. Using a $1.0R_{\oplus}$ Earth-sized planet transiting a 3200 K, $0.155R_{\odot}$ M4V dwarf star with $i = 90.0^{\circ}$ and $P = 2$ d. The starspot properties are: $\theta = 0^{\circ}$, $\phi = 90^{\circ}$, $r_{\text{spot}} = 0.061R_{*}$ and $T_{\text{spot}} = 3150$ K. The observational wavelength and the rms scatter for the simulated data were set at 785 nm and 200 ± 10 ppm respectively. The solid line represents the noise-free synthetic light curve containing the starspot anomaly, while, the filled circles represent the “spot-free” synthetic light curve (see Section 3) with added Gaussian noise.

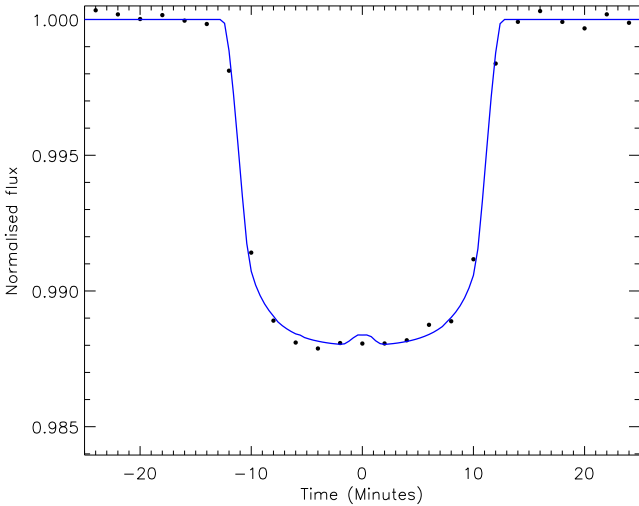


Fig. 10. Example of multiple data points describing the plateau of a starspot anomaly. Using a $1.75R_{\oplus}$ super-Earth planet transiting a 3200 K, $0.155R_{\odot}$ M4V dwarf star with $i = 90.0^{\circ}$ and $P = 2$ d. The starspot properties are: $\theta = 0^{\circ}$, $\phi = 90^{\circ}$, $r_{\text{spot}} = 0.061R_{*}$ and $T_{\text{spot}} = 3150$ K. The observational wavelength and the rms scatter for the simulated data were set at 785 nm and 200 ± 10 ppm respectively. The solid line represents the noise-free synthetic light curve containing the starspot anomaly, while, the filled circles represent the “spot-free” synthetic light curve (see Section 3) with added Gaussian noise.

point should require a larger amplitude (compared to multiple data points) to allow a confirmed starspot detection. However, this creates an unavoidable detection bias.

Fig. 9 & Fig. 10 depict two identical scenarios except that they have two different R_p , $R_p = 1.0 R_{\oplus}$ (Fig. 9) and $R_p = 1.75 R_{\oplus}$ (Fig. 10). The starspot ($r_{\text{spot}} = 0.061R_{*}$) is not detected in Fig. 9, however, by increasing the duration of the starspot anomaly,

and therefore, the number of data points which describe it, the starspot is then detected (Fig. 10).

The mean amplitude of the starspot anomalies are 205 ppm (Fig. 9) and 394 ppm (Fig. 10). This shows how by increasing the duration of starspot anomaly, can allow for its detection and explains why large planets are needed to detect starspots which are both small and hot in TESS transit light curves.

3.6. Comparing the change in flux between the planet and starspot

The values of R_p and \bar{r}_{spot} given in Table 3, while are valuable, don’t allow for a direct comparison between the three host star spectral types. To allow a direct comparison, R_p and \bar{r}_{spot} need to be converted into change in flux (ΔF). R_p can be converted to ΔF_p using k^2 where:

$$\Delta F_p = k^2 = \left(\frac{R_p}{R_*}\right)^2, \quad (4)$$

which gives the area of the planetary disc in units of a uniform stellar disc. Because the simulations used in this work examined starspot occultations when the starspot was at the centre of the stellar disc, we can use this approximation of ΔF_p in the absence of limb darkening.

The surface area of the starspot is the solid angle, Ω and using r_{spot} as the angular radius of the starspot, is given by:

$$\Omega = 2\pi R_*^2 (1 - \cos r_{\text{spot}}), \quad (5)$$

which in units of the stellar hemisphere ($2\pi R_*^2$) becomes:

$$\frac{\Omega}{2\pi R_*^2} = (1 - \cos r_{\text{spot}}). \quad (6)$$

However, unlike the planet, the starspot emits a flux which means that the flux deficit caused by the starspot, ΔF_{spot} is related to r_{spot} by ρ_{spot} using the following relation:

$$\Delta F_{\text{spot}} = (1 - \cos r_{\text{spot}})(1 - \rho_{\text{spot}}) \quad (7)$$

For the simulations in this work 36 different values of ρ_{spot} were used. These were derived using Eq. 2 using three values of T_{eff} , four T_{spot} and three λ_{obs} . This equates to 12 different values of ρ_{spot} for each stellar spectral class. To determine ΔF_{spot} , the mean starspot contrast ($\bar{\rho}_{\text{spot}}$) was calculated for each spectral class and are given in Table 4.

Therefore ΔF_{spot} was calculated for the nine \bar{r}_{spot} (Table 3) for each spectral class using the associated $\bar{\rho}_{\text{spot}}$ (Table 4). The resultant calculated values of ΔF_p (Eq. 4) and ΔF_{spot} (Eq. 7) are given in Fig. 11 & 12.

Fig. 11 shows that the results for each of the three host stars are in excellent agreement with each other in terms of the smallest ΔF_{spot} that can be detected. The simulation results indicate that when $k \geq 0.10$ then a starspot will need a larger ΔF_{spot} to be detected, either by increasing r_{spot} or ρ_{spot} . The positive gradient towards larger ΔF_p represents that larger planets can only detect larger or cooler starspots. The steep negative gradient towards smaller ΔF_p shows that the effect from using a fixed cadence

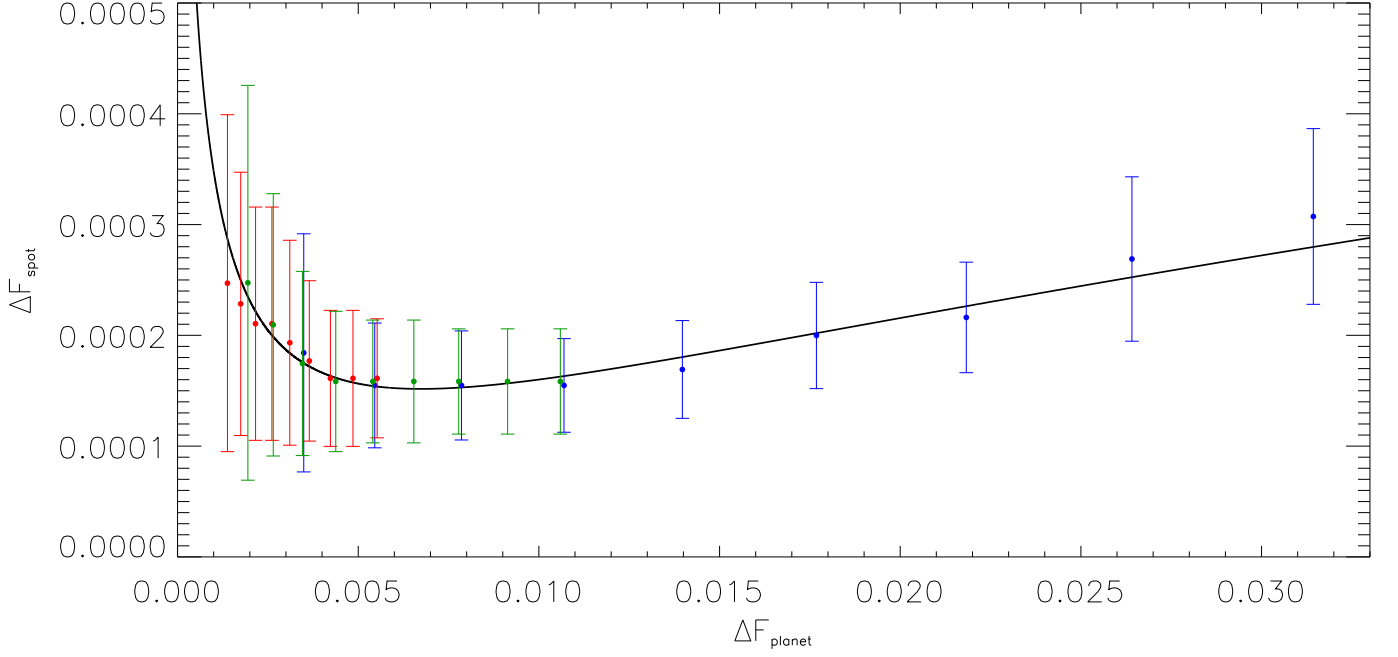


Fig. 11. Plot of ΔF_p and ΔF_{spot} calculated from Eq. 4 & 7 combined with the best fitting model (solid black line). The blue data points represent the M4V host star results. The red data points represent the M1V host star results, while, the green data points represent the K5V host star results.

Table 4. The 36 values of ρ_{spot} used in the simulations and the three calculated $\bar{\rho}_{\text{spot}}$ for the M4V, M1V and K5V host star simulations (highlighted in bold).

M4V			M1V			K5V		
$T_{\text{eff}} = 3200 \text{ K}$			$T_{\text{eff}} = 3700 \text{ K}$			$T_{\text{eff}} = 4100 \text{ K}$		
T_{spot} (K)	λ_{obs} (nm)	ρ_{spot}	T_{spot} (K)	λ_{obs} (nm)	ρ_{spot}	T_{spot} (K)	λ_{obs} (nm)	ρ_{spot}
600	0.61		600	0.56		600	0.53	
3000	0.68		3400	0.64		3700	0.61	
1000	0.74		1000	0.70		1000	0.68	
600	0.69		600	0.66		600	0.63	
3050	0.75		3475	0.72		3800	0.70	
1000	0.80		1000	0.77		1000	0.75	
600	0.78		600	0.76		600	0.74	
3100	0.83		3550	0.81		3900	0.79	
1000	0.86		1000	0.85		1000	0.83	
600	0.89		600	0.87		600	0.86	
3150	0.91		3625	0.90		4000	0.89	
1000	0.93		1000	0.92		1000	0.91	
0.79			0.76			0.74		

combined with the method that is used to detect starspot anomalies, has a stronger influence on the size of starspot which can be detected in TESS transit light curves.

To determine which ΔF_p will allow for the smallest ΔF_{spot} to be detected, we fitted a parametrised 2nd order polynomial to the results. This was accomplished by parametrising ΔF_p to a logarithmic scale:

$$t = \log_{10} \left(\frac{1}{\Delta F_p} \right), \quad (8)$$

where t is the logarithmic parametrisation of ΔF_p .

Fig. 12 shows the comparison between t and ΔF_{spot} which indicates a quadratic relation, between the two quantities. We use MCMC to fit a quadratic relation:

$$\Delta F_{\text{spot}} = (0.00028 \pm 0.00001)t^2 - (0.00121 \pm 0.00001)t + (0.00147 \pm 0.00002) \quad (9)$$

Using Eq. 9 and setting $\frac{d\Delta F_{\text{spot}}}{dt} = 0$ we find that the smallest detectable $\Delta F_{\text{spot}} = 0.00015 \pm 0.00001$, when $\Delta F_p = 0.0067 \pm 0.0006$ ($k = 0.082 \pm 0.004$). This allows us to determine that for a $1 R_{\oplus}$ planet, a host star with $R_* = 0.112 \pm 0.005 R_{\odot}$ will be required to detect starspots with $\Delta F_{\text{spot}} = 0.00015 \pm 0.00001$. While for a $3 R_{\oplus}$ sub-Neptune planet, a host star with $R_* = 0.335 \pm 0.015 R_{\odot}$ will be required to find starspots with $\Delta F_{\text{spot}} = 0.00015 \pm 0.00001$.

In Section 2.2 we describe how a degeneracy exists between r_{spot} and ρ_{spot} . For the simulations performed in this work, the smallest r_{spot} was determined for sets of fixed parameter values, which included ρ_{spot} (calculated from T_{spot} , T_{eff} and λ_{obs} using Eq. 2). Table 4 gives the range of ρ_{spot} used in the simulations (0.53–0.93) and when combined with the results given in Tables A.1, A.2 and A.3 allows an extrapolation, to determine the largest ρ_{spot} for a fixed r_{spot} .

However, Eq. 9 can be used to determine the largest average detectable ρ_{spot} for a fixed r_{spot} . For a $1 R_{\text{Jup}}$ planet, transiting a $1 R_{\odot}$ star, the change in flux caused by the transiting planet is $\Delta F_p \approx 0.01$. When parametrised using Eq. 8 gives, $t = 2$. Eq. 9 then calculates the smallest detectable ΔF_{spot} for the system, $\Delta F_{\text{spot}} = 0.000166 \pm 0.00006$. Using Eq. 7 with a given starspot angular radius, $r_{\text{spot}} = 5^\circ$ ($r_{\text{spot}} = 0.087 R_*$) we can determine the lowest contrast detectable in TESS transit light curves for the starspot, $\rho_{\text{spot}} = 0.96 \pm 0.02$. While for a $r_{\text{spot}} = 2^\circ$ ($r_{\text{spot}} = 0.035 R_*$) we find the lowest contrast detectable to be $\rho_{\text{spot}} = 0.73 \pm 0.10$. For a $r_{\text{spot}} = 1^\circ$ ($r_{\text{spot}} = 0.017 R_*$) Eq. 7 gives

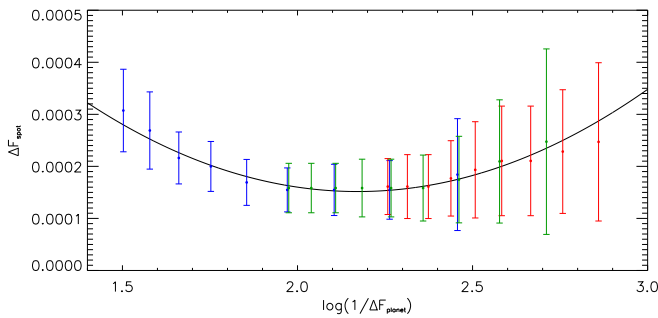


Fig. 12. Plot of $\log_{10}\left(\frac{1}{\Delta F_p}\right)$ and ΔF_{spot} calculated from Eq. 4 & 7 combined with the best fitting model (solid black line). The blue data points represent the M4V host star results. The red data points represent the M1V host star results, while, the green data points represent the K5V host star results.

a negative value for ρ_{spot} , indicating that it is not possible for a $r_{\text{spot}} = 0.017R_*$ starspot to be detected in TESS transit data of a $1 R_{\text{Jup}}$ planet, transiting a $1 R_{\odot}$ star.

4. Discussion and Conclusions

The key result from the simulations performed in this work indicate that when TESS observes a transiting planet that occults a starspot on the stellar disc, the characteristic “blip” of the starspot anomaly will be seen in the resulting light curve. This removes the doubt that starspot anomalies will be present in TESS light curves (due to the TESS primary targets being cooler (redder) host stars with shorter transit durations.) and opens the possibility of using the starspot tracking technique (e.g., Tregloan-Reed et al. 2013, 2015; Mohler-Fischer et al. 2013; Southworth et al. 2016; Mancini et al. 2017) to measure the orbital obliquity of TESS planetary systems. Particularly for targets where the conventional Rossiter-McLaughlin technique (Rossiter 1924; McLaughlin 1924; Schlesinger 1910, 1916; Holt 1893) is not viable (e.g., slow-rotators, small k and active stars). The simulations then go further in determining the detection limits for a variety of starspot temperatures, planetary & stellar radii, photometric precision, orbital periods and observational wavelengths. It was found that the starspot detection limits in TESS light curves for M4V, M1V and K5V host stars were 4900 ± 1700 km, 13800 ± 6000 km and 15900 ± 6800 km respectively.

The simulations confirmed expected trends in the detection limits of starspot anomalies, including the photometric parameter dependences of the amplitude of the starspot anomaly. The result confirmed that the amplitude of a starspot anomaly is strongly dependent on r_{spot} and ρ_{spot} , and therefore, by association with ρ_{spot} , strongly dependent on T_{eff} and λ_{obs} . While, the amplitude of the starspot anomaly is less dependent on P . The simulations then show that overall the detection limit of a starspot anomaly is dependent on R_p (Table 3) and is therefore dependent on, ΔF_{planet} . However, the simulations uncovered an unexpected trend: starspots which are small and hot can be detected by large planets, however, they can’t be detected by smaller planets.

From our investigations of the synthetic light curves, we uncovered that the unexpected trend was a detection bias, generated by the fixed 2 min cadence of TESS combined with the method used to determine if the starspot anomaly was detectable, by comparing the mean amplitude of a starspot anomaly to the observational noise. This detection method is in agreement with fit-

ting starspot anomalies in transit light curves. If the mean amplitude of the starspot anomaly is not large enough, it is not possible to constrain the starspot properties (see Section 3). It was found that for anomalies with a short maximum duration (apex shape) the data points lying on the ingress and egress of the starspot anomaly reduced the mean amplitude. As a consequence for the starspot to be detected either r_{spot} or R_p needed to be increased to increase the mean amplitude. Though as in the case depicted in Fig. 4, if the maximum amplitude of the starspot anomaly is below the detection threshold, then increasing r_{spot} further did not allow a detection. If instead of using the mean amplitude, the maximum amplitude was tested against the rms scatter in the data, it would allow starspot anomalies described by a single data point (i.e., apex shape) to be considered detected, when in reality would be dismissed as noise (e.g., Fig. 9). By using the mean amplitude of the starspot anomaly, effectively mimics what happens when a transit-starspot model fits a starspot anomaly. Hence, the unexpected trend – smaller hot starspots will be detected by larger planets – will be present when analysing TESS transit light curves. To counter this would require a reduction in the observational cadence, which would increase the number of data points which describe the starspot anomaly. However, this is not practical when analysing TESS transit data and would require further follow-up photometric observations using a different telescope.

By separating the simulations into three groups for each of the three host stars and then converting R_p and \bar{r}_{spot} into ΔF_{planet} and ΔF_{spot} , a direct comparison between the planets and starspots for the three host stars was made. The resultant comparison between ΔF_{planet} and ΔF_{spot} showed excellent agreement of the simulations between the three host stars and indicate that the smallest and hottest starspots detected in TESS transit light curves will be when $k = 0.082 \pm 0.004$. By fitting a parametrised 2nd order polynomial to the results, we are able to determine the minimum size and lowest contrast (highest intensity) that can be detected for a given value of k in the TESS exoplanetary transit data. The comparison also revealed that the effect from using a fixed 2 min cadence combined to using the mean flux of a starspot anomaly to determine its detection had a larger impact on ΔF_{spot} than R_p .

Young K and M dwarf stars are known to have a high starspot surface coverage (e.g., O’Neal et al. 2004; Jackson & Jeffries 2013). However, the activity-age relationship is still unknown. This leads to the question, how many TESS transit light curves will contain starspot anomalies. The simulations presented in this work are the starting point, in beginning to answer this question. In that the simulations show that starspot anomalies will be observable in TESS transit light curves. The starspot distribution on the stellar disc will also be an important factor in this question. Barnes et al. (2015) used high resolution Doppler images of two M dwarfs (GJ 791.2 A; M4.5: LP 944-20; M9) to determine the overall starspot filling factors $\approx 3\%$ and $\approx 1.5\%$ for the two M dwarfs. However, Barnes et al. (2015) found maximum starspot filling factors 82.3% and 76.6% at high latitudes (polar). If the starspot distributions of GJ 791.2 A and LP 944-20 can be considered typical of M dwarf stars that will be observed by TESS. Then a polar biased starspot distribution will affect the total number of TESS transit light curves, which contain a starspot anomaly. By determining the smallest detectable starspot size for a range of planetary sizes, starspot temperatures, orbital periods and noise levels is an essential first step in beginning to forecast the number of TESS transit light curves which will be affected by starspot anomalies. Therefore, gauging the importance and the community future reliance on transit-starspot models.

Acknowledgements. We would like to thank the anonymous referee and the editor for their helpful comments, which improved the quality of this manuscript. This work was supported by a CONICYT / FONDECYT 2018 Postdoctoral research grant, project number: 3180071. JTR thanks the Centro de Astronomía (CITEVA), Universidad de Antofagasta for hosting the CONICYT / FONDECYT 2018 Postdoctoral research grant. The following internet-based resources were used in the research for this paper: the NASA Astrophysics Data System; the SIMBAD database and VizieR catalogue access tool operated at CDS, Strasbourg, France; and the arXiv scientific paper preprint service operated by Cornell University.

References

- Ballerini, P., Micela, G., Lanza, A. F., & Pagano, I. 2012, *A&A*, 539, A140
- Barnes, J. R., Jeffers, S. V., Jones, H. R. A., et al. 2015, *ApJ*, 812, 42
- Bayliss, D., Gillen, E., Eiglmüller, P., et al. 2018, *MNRAS*, 475, 4467
- Béky, B., Kipping, D. M., & Holman, M. J. 2014, *MNRAS*, 442, 3686
- Borucki, W. J., Koch, D., Basri, G., et al. 2010, *Science*, 327, 977
- Boyajian, T. S., von Braun, K., van Belle, G., et al. 2012, *ApJ*, 757, 112
- Chen, G., Guenther, E. W., Pallé, E., et al. 2017, *A&A*, 600, A138
- Claret, A. 2017, *A&A*, 600, A30
- Dotter, A., Chaboyer, B., Jevremović, D., et al. 2008, *ApJS*, 178, 89
- Dragomir, D., Teske, J., Gunther, M. N., et al. 2018 [[arXiv:1901.00051](#)]
- Dressing, C. D. & Charbonneau, D. 2013, *ApJ*, 767, 95
- Dressing, C. D. & Charbonneau, D. 2015, *ApJ*, 807, 45
- Fortney, J. J., Marley, M. S., & Barnes, J. W. 2007, *ApJ*, 659, 1661
- Hartman, J. D., Bayliss, D., Brahm, R., et al. 2015, *AJ*, 149, 166
- Herrero, E., Ribas, I., Jordi, C., et al. 2016, *A&A*, 586, A131
- Holt, J. R. 1893, *Astronomy and Astro-Physics*, 12
- Huang, C. X., Burt, J., Vanderburg, A., et al. 2018, *ApJ*, 868, L39
- Jackson, R. J. & Jeffries, R. D. 2013, *MNRAS*, 431, 1883
- Jenkins, J. M., Twicken, J. D., McCauliff, S., et al. 2016, in *Proc. SPIE*, Vol. 9913, *Software and Cyberinfrastructure for Astronomy IV*, 99133E
- Johnson, J. A., Gazak, J. Z., Apps, K., et al. 2012, *AJ*, 143, 111
- Juvan, I. G., Lendl, M., Cubillos, P. E., et al. 2018, *A&A*, 610, A15
- Kopparapu, R. K., Ramirez, R., Kasting, J. F., et al. 2013, *ApJ*, 765, 131
- Mancini, L., Ciceri, S., Chen, G., et al. 2013, *MNRAS*, 436, 2
- Mancini, L., Esposito, M., Covino, E., et al. 2015, *A&A*, 579, A136
- Mancini, L., Southworth, J., Ciceri, S., et al. 2014, *MNRAS*, 443, 2391
- Mancini, L., Southworth, J., Raia, G., et al. 2017, *MNRAS*, 465, 843
- Maxted, P. F. L. 2016, *A&A*, 591, A111
- McLaughlin, D. B. 1924, *ApJ*, 60, 22
- Mohler-Fischer, M., Mancini, L., Hartman, J. D., et al. 2013, *A&A*, 558, A55
- Montalto, M., Boué, G., Oshagh, M., et al. 2014, *MNRAS*, 444, 1721
- Morton, T. D. & Swift, J. 2014, *ApJ*, 791, 10
- Nikolov, N., Chen, G., Fortney, J. J., et al. 2013, *A&A*, 553, A26
- O’Neal, D., Neff, J. E., Saar, S. H., & Cuntz, M. 2004, *AJ*, 128, 1802
- Oshagh, M., Boisse, I., Boué, G., et al. 2013, *A&A*, 549, A35
- Prša, A., Conroy, K. E., Horvat, M., et al. 2016, *ApJS*, 227, 29
- Prša, A. & Zwitter, T. 2005, *ApJ*, 628, 426
- Rabus, M., Alonso, R., Belmonte, J. A., et al. 2009, *A&A*, 494, 391
- Ricker, G. R., Latham, D. W., Vanderspek, R. K., et al. 2009, in *Bulletin of the American Astronomical Society*, Vol. 41, American Astronomical Society Meeting Abstracts #213, 193
- Ricker, G. R., Winn, J. N., Vanderspek, R., et al. 2014, in *Space Telescopes and Instrumentation 2014: Optical, Infrared, and Millimeter Wave*, Vol. 9143, 914320
- Ricker, G. R., Winn, J. N., Vanderspek, R., et al. 2015, *Journal of Astronomical Telescopes, Instruments, and Systems*, 1, 014003
- Rossiter, R. A. 1924, *ApJ*, 60, 15
- Sanchis-Ojeda, R., Fabrycky, D. C., Winn, J. N., et al. 2012, *Nature*, 487, 449
- Sanchis-Ojeda, R. & Winn, J. N. 2011, *ApJ*, 743, 61
- Sanchis-Ojeda, R., Winn, J. N., Holman, M. J., et al. 2011, *ApJ*, 733, 127
- Sanchis-Ojeda, R., Winn, J. N., Marcy, G. W., et al. 2013, *ApJ*, 775, 54
- Schlesinger, F. 1910, *Publications of the Allegheny Observatory of the University of Pittsburgh*, 1, 123
- Schlesinger, F. 1916, *Publications of the Allegheny Observatory of the University of Pittsburgh*, 3, 23
- Silva, A. V. R. 2003, *ApJ*, 585, L147
- Silva-Válio, A. 2010, in *IAU Symposium*, Vol. 264, IAU Symposium, ed. A. G. Kosovichev, A. H. Andrei, & J.-P. Roelot, 440–442
- Silva-Valio, A., Lanza, A. F., Alonso, R., & Barge, P. 2010, *A&A*, 510, A25
- Southworth, J. 2008, *MNRAS*, 386, 1644
- Southworth, J. 2010, *MNRAS*, 408, 1689
- Southworth, J. 2011, *MNRAS*, 417, 2166
- Southworth, J. 2013, *A&A*, 557, A119
- Southworth, J., Bruntt, H., & Buzasi, D. L. 2007, *A&A*, 467, 1215
- Southworth, J., Hinse, T. C., Dominik, M., et al. 2009, *ApJ*, 707, 167
- Southworth, J., Maxted, P. F. L., & Smalley, B. 2004, *MNRAS*, 351, 1277
- Southworth, J., Smalley, B., Maxted, P. F. L., Claret, A., & Etzel, P. B. 2005, *MNRAS*, 363, 529
- Southworth, J., Tregloan-Reed, J., Andersen, M. I., et al. 2016, *MNRAS*, 457, 4205
- Stassun, K. G., Oelkers, R. J., Pepper, J., et al. 2018, *AJ*, 156, 102
- Sullivan, P. W., Winn, J. N., Berta-Thompson, Z. K., et al. 2015, *ApJ*, 809, 77
- Sullivan, P. W., Winn, J. N., Berta-Thompson, Z. K., et al. 2017, *ApJ*, 837, 99
- Tregloan-Reed, J., Southworth, J., Burgdorf, M., et al. 2015, *MNRAS*, 450, 1760
- Tregloan-Reed, J., Southworth, J., Mancini, L., et al. 2018, *MNRAS*, 474, 5485
- Tregloan-Reed, J., Southworth, J., & Tappert, C. 2013, *MNRAS*, 428, 3671
- Valio, A., Estrela, R., Netto, Y., Bravo, J. P., & de Medeiros, J. R. 2017, *ApJ*, 835, 294
- Vanderspek, R., Huang, C. X., Vanderburg, A., et al. 2019, *ApJ*, 871, L24
- Wang, S., Jones, M., Shporer, A., et al. 2019, *AJ*, 157, 51
- Wheatley, P. J., Pollacco, D. L., Queloz, D., et al. 2013, in *European Physical Journal Web of Conferences*, Vol. 47, European Physical Journal Web of Conferences, 13002
- Wilson, R. E. 1979, *ApJ*, 234, 1054
- Wilson, R. E. 1990, *ApJ*, 356, 613
- Wilson, R. E. 2008, *ApJ*, 672, 575
- Wilson, R. E. 2012, *AJ*, 144, 73
- Wilson, R. E. & Devinney, E. J. 1971, *ApJ*, 166, 605
- Winn, J. N. 2010, *Exoplanet Transits and Occultations*, ed. S. Seager (University of Arizona Press), 55–77

Appendix A: Full results of all simulations

Table A.1. The smallest detectable value of r_{spot} determined from the 6718 simulations of the 1296 scenarios that used an M4V dwarf host star.

T_{spot} (K)	rms scatter (ppm)	$\lambda_{\text{obs}} = 600 \text{ nm}$			$\lambda_{\text{obs}} = 785 \text{ nm}$			$\lambda_{\text{obs}} = 1000 \text{ nm}$		
		P			P			P		
		1 d	2 d	3 d	1 d	2 d	3 d	1 d	2 d	3 d
$R_p = 1.00 R_{\oplus}$										
3000	60	0.017 R_*	0.026 R_*	0.026 R_*	0.017 R_*	0.026 R_*	0.026 R_*	0.026 R_*	0.026 R_*	0.026 R_*
3000	100	0.026 R_*	0.026 R_*	0.035 R_*	0.026 R_*	0.035 R_*	0.035 R_*	0.026 R_*	0.035 R_*	0.044 R_*
3000	150	0.026 R_*	0.035 R_*	0.044 R_*	0.035 R_*	0.035 R_*	0.044 R_*	0.035 R_*	0.044 R_*	0.044 R_*
3000	200	0.035 R_*	0.035 R_*	0.044 R_*	0.035 R_*	0.044 R_*	0.052 R_*	0.044 R_*	0.052 R_*	0.052 R_*
3050	60	0.017 R_*	0.026 R_*	0.026 R_*	0.026 R_*	0.026 R_*	0.026 R_*	0.026 R_*	0.026 R_*	0.035 R_*
3050	100	0.026 R_*	0.035 R_*	0.035 R_*	0.026 R_*	0.035 R_*	0.044 R_*	0.035 R_*	0.044 R_*	0.044 R_*
3050	150	0.035 R_*	0.044 R_*	0.044 R_*	0.035 R_*	0.044 R_*	0.052 R_*	0.044 R_*	0.052 R_*	0.052 R_*
3050	200	0.035 R_*	0.044 R_*	0.052 R_*	0.044 R_*	0.052 R_*	0.061 R_*	0.044 R_*	0.061 R_*	0.061 R_*
3100	60	0.026 R_*	0.026 R_*	0.035 R_*	0.026 R_*	0.026 R_*	0.035 R_*	0.026 R_*	0.035 R_*	0.044 R_*
3100	100	0.035 R_*	0.035 R_*	0.044 R_*	0.035 R_*	0.044 R_*	0.052 R_*	0.044 R_*	0.044 R_*	0.052 R_*
3100	150	0.044 R_*	0.044 R_*	0.052 R_*	0.044 R_*	0.052 R_*	0.061 R_*	0.052 R_*	0.061 R_*	0.061 R_*
3100	200	0.044 R_*	0.052 R_*	0.061 R_*	0.052 R_*	0.061 R_*	0.079 R_*	0.061 R_*	0.070 R_*	0.096 R_*
3150	60	0.035 R_*	0.035 R_*	0.044 R_*	0.035 R_*	0.044 R_*	0.052 R_*	0.044 R_*	0.052 R_*	0.052 R_*
3150	100	0.044 R_*	0.052 R_*	0.061 R_*	0.052 R_*	0.061 R_*	0.070 R_*	0.061 R_*	0.079 R_*	0.087 R_*
3150	150	0.052 R_*	0.070 R_*	0.079 R_*	0.070 R_*	0.096 R_*	0.105 R_*	0.113 R_*	0.140 R_*	0.140 R_*
3150	200	0.079 R_*	0.096 R_*	0.105 R_*	0.122 R_*	0.157 R_*	0.209 R_*	NaN	NaN	NaN
$R_p = 1.25 R_{\oplus}$										
3000	60	0.017 R_*	0.017 R_*	0.026 R_*	0.017 R_*	0.026 R_*	0.026 R_*	0.026 R_*	0.026 R_*	0.026 R_*
3000	100	0.026 R_*	0.026 R_*	0.035 R_*	0.026 R_*	0.026 R_*	0.035 R_*	0.026 R_*	0.035 R_*	0.035 R_*
3000	150	0.026 R_*	0.035 R_*	0.035 R_*	0.035 R_*	0.035 R_*	0.035 R_*	0.035 R_*	0.035 R_*	0.044 R_*
3000	200	0.035 R_*	0.035 R_*	0.044 R_*	0.035 R_*	0.044 R_*	0.044 R_*	0.035 R_*	0.044 R_*	0.052 R_*
3050	60	0.017 R_*	0.026 R_*	0.026 R_*	0.026 R_*	0.026 R_*	0.026 R_*	0.026 R_*	0.026 R_*	0.026 R_*
3050	100	0.026 R_*	0.026 R_*	0.035 R_*	0.035 R_*	0.035 R_*	0.035 R_*	0.035 R_*	0.035 R_*	0.044 R_*
3050	150	0.035 R_*	0.035 R_*	0.044 R_*	0.035 R_*	0.035 R_*	0.044 R_*	0.035 R_*	0.044 R_*	0.052 R_*
3050	200	0.035 R_*	0.044 R_*	0.044 R_*	0.035 R_*	0.044 R_*	0.052 R_*	0.044 R_*	0.052 R_*	0.052 R_*
3100	60	0.026 R_*	0.026 R_*	0.026 R_*	0.026 R_*	0.026 R_*	0.035 R_*	0.026 R_*	0.035 R_*	0.035 R_*
3100	100	0.035 R_*	0.035 R_*	0.035 R_*	0.035 R_*	0.035 R_*	0.044 R_*	0.035 R_*	0.044 R_*	0.044 R_*
3100	150	0.044 R_*	0.035 R_*	0.044 R_*	0.044 R_*	0.044 R_*	0.052 R_*	0.044 R_*	0.052 R_*	0.061 R_*
3100	200	0.044 R_*	0.044 R_*	0.052 R_*	0.052 R_*	0.052 R_*	0.061 R_*	0.052 R_*	0.061 R_*	0.070 R_*
3150	60	0.035 R_*	0.035 R_*	0.035 R_*	0.035 R_*	0.035 R_*	0.044 R_*	0.044 R_*	0.044 R_*	0.044 R_*
3150	100	0.044 R_*	0.044 R_*	0.052 R_*	0.052 R_*	0.052 R_*	0.061 R_*	0.052 R_*	0.061 R_*	0.061 R_*
3150	150	0.052 R_*	0.061 R_*	0.061 R_*	0.061 R_*	0.070 R_*	0.079 R_*	0.061 R_*	0.079 R_*	0.096 R_*
3150	200	0.061 R_*	0.070 R_*	0.079 R_*	0.070 R_*	0.079 R_*	0.096 R_*	0.087 R_*	0.096 R_*	0.122 R_*
$R_p = 1.50 R_{\oplus}$										
3000	60	0.026 R_*	0.026 R_*	0.026 R_*	0.026 R_*	0.026 R_*	0.026 R_*	0.026 R_*	0.026 R_*	0.026 R_*
3000	100	0.026 R_*	0.026 R_*	0.026 R_*	0.026 R_*	0.026 R_*	0.035 R_*	0.026 R_*	0.026 R_*	0.035 R_*
3000	150	0.026 R_*	0.026 R_*	0.035 R_*	0.035 R_*	0.035 R_*	0.035 R_*	0.035 R_*	0.035 R_*	0.044 R_*
3000	200	0.035 R_*	0.035 R_*	0.035 R_*	0.035 R_*	0.035 R_*	0.044 R_*	0.044 R_*	0.044 R_*	0.044 R_*
3050	60	0.026 R_*	0.026 R_*	0.026 R_*	0.026 R_*	0.026 R_*	0.026 R_*	0.026 R_*	0.026 R_*	0.035 R_*
3050	100	0.026 R_*	0.026 R_*	0.035 R_*	0.026 R_*	0.026 R_*	0.035 R_*	0.035 R_*	0.035 R_*	0.035 R_*
3050	150	0.035 R_*	0.035 R_*	0.035 R_*	0.035 R_*	0.035 R_*	0.044 R_*	0.044 R_*	0.044 R_*	0.044 R_*
3050	200	0.035 R_*	0.035 R_*	0.044 R_*	0.044 R_*	0.044 R_*	0.044 R_*	0.044 R_*	0.044 R_*	0.052 R_*
3100	60	0.026 R_*	0.026 R_*	0.035 R_*	0.026 R_*	0.035 R_*	0.035 R_*	0.035 R_*	0.035 R_*	0.035 R_*
3100	100	0.035 R_*	0.035 R_*	0.035 R_*	0.035 R_*	0.035 R_*	0.044 R_*	0.044 R_*	0.044 R_*	0.044 R_*
3100	150	0.044 R_*	0.044 R_*	0.044 R_*	0.044 R_*	0.044 R_*	0.044 R_*	0.044 R_*	0.044 R_*	0.052 R_*
3100	200	0.044 R_*	0.044 R_*	0.052 R_*	0.044 R_*	0.052 R_*	0.052 R_*	0.052 R_*	0.052 R_*	0.061 R_*
3150	60	0.035 R_*	0.035 R_*	0.044 R_*	0.044 R_*	0.044 R_*	0.044 R_*	0.044 R_*	0.044 R_*	0.052 R_*
3150	100	0.044 R_*	0.044 R_*	0.052 R_*	0.044 R_*	0.052 R_*	0.052 R_*	0.052 R_*	0.052 R_*	0.061 R_*
3150	150	0.052 R_*	0.052 R_*	0.061 R_*	0.061 R_*	0.061 R_*	0.070 R_*	0.061 R_*	0.070 R_*	0.079 R_*
3150	200	0.061 R_*	0.061 R_*	0.070 R_*	0.070 R_*	0.070 R_*	0.079 R_*	0.079 R_*	0.079 R_*	0.087 R_*
$R_p = 1.75 R_{\oplus}$										
3000	60	0.026 R_*	0.026 R_*	0.026 R_*	0.026 R_*	0.026 R_*	0.026 R_*	0.026 R_*	0.026 R_*	0.026 R_*
3000	100	0.026 R_*	0.026 R_*	0.026 R_*	0.026 R_*	0.026 R_*	0.026 R_*	0.026 R_*	0.026 R_*	0.026 R_*
3000	150	0.026 R_*	0.026 R_*	0.026 R_*	0.035 R_*	0.035 R_*	0.035 R_*	0.035 R_*	0.035 R_*	0.035 R_*
3000	200	0.035 R_*	0.035 R_*	0.035 R_*	0.035 R_*	0.035 R_*	0.035 R_*	0.035 R_*	0.044 R_*	0.044 R_*
3050	60	0.026 R_*	0.026 R_*	0.026 R_*	0.026 R_*	0.026 R_*	0.026 R_*	0.026 R_*	0.026 R_*	0.035 R_*
3050	100	0.026 R_*	0.026 R_*	0.035 R_*	0.026 R_*	0.026 R_*	0.035 R_*	0.035 R_*	0.035 R_*	0.035 R_*
3050	150	0.035 R_*	0.035 R_*	0.035 R_*	0.035 R_*	0.035 R_*	0.044 R_*	0.044 R_*	0.044 R_*	0.044 R_*
3050	200	0.035 R_*	0.035 R_*	0.044 R_*	0.044 R_*	0.044 R_*	0.044 R_*	0.044 R_*	0.044 R_*	0.052 R_*
3100	60	0.026 R_*	0.026 R_*	0.035 R_*	0.026 R_*	0.035 R_*	0.035 R_*	0.035 R_*	0.035 R_*	0.035 R_*
3100	100	0.035 R_*	0.035 R_*	0.035 R_*	0.035 R_*	0.035 R_*	0.044 R_*	0.044 R_*	0.044 R_*	0.044 R_*
3100	150	0.044 R_*	0.044 R_*	0.044 R_*	0.044 R_*	0.044 R_*	0.044 R_*	0.044 R_*	0.044 R_*	0.052 R_*
3100	200	0.044 R_*	0.044 R_*	0.052 R_*	0.044 R_*	0.052 R_*	0.052 R_*	0.052 R_*	0.052 R_*	0.061 R_*
3150	60	0.035 R_*	0.035 R_*	0.044 R_*	0.044 R_*	0.044 R_*	0.044 R_*	0.044 R_*	0.044 R_*	0.052 R_*
3150	100	0.044 R_*	0.044 R_*	0.052 R_*	0.044 R_*	0.052 R_*	0.052 R_*	0.052 R_*	0.052 R_*	0.061 R_*
3150	150	0.052 R_*	0.052 R_*	0.061 R_*	0.061 R_*	0.061 R_*	0.070 R_*	0.061 R_*	0.070 R_*	0.079 R_*
3150	200	0.061 R_*	0.061 R_*	0.070 R_*	0.070 R_*	0.070 R_*	0.079 R_*	0.079 R_*	0.079 R_*	0.087 R_*

3050	100	0.026R _*	0.026R _*	0.026R _*	0.026R _*	0.026R _*	0.026R _*	0.035R _*	0.035R _*	0.035R _*
3050	150	0.035R _*	0.035R _*	0.035R _*	0.035R _*	0.035R _*	0.035R _*	0.035R _*	0.035R _*	0.044R _*
3050	200	0.035R _*	0.035R _*	0.035R _*	0.044R _*	0.044R _*	0.044R _*	0.044R _*	0.044R _*	0.044R _*
3100	60	0.035R _*	0.035R _*	0.035R _*	0.035R _*	0.035R _*	0.035R _*	0.035R _*	0.035R _*	0.044R _*
3100	100	0.035R _*	0.035R _*	0.035R _*	0.035R _*	0.035R _*	0.035R _*	0.035R _*	0.035R _*	0.044R _*
3100	150	0.035R _*	0.035R _*	0.035R _*	0.044R _*	0.044R _*	0.044R _*	0.044R _*	0.044R _*	0.052R _*
3100	200	0.044R _*	0.044R _*	0.044R _*	0.044R _*	0.052R _*	0.052R _*	0.052R _*	0.052R _*	0.061R _*
3150	60	0.044R _*	0.044R _*	0.044R _*	0.044R _*	0.044R _*	0.052R _*	0.052R _*	0.052R _*	0.052R _*
3150	100	0.044R _*	0.044R _*	0.044R _*	0.044R _*	0.052R _*	0.052R _*	0.052R _*	0.052R _*	0.061R _*
3150	150	0.052R _*	0.052R _*	0.052R _*	0.052R _*	0.052R _*	0.061R _*	0.061R _*	0.070R _*	0.070R _*
3150	200	0.052R _*	0.061R _*	0.061R _*	0.061R _*	0.061R _*	0.070R _*	0.070R _*	0.079R _*	0.079R _*
R _p = 2.00R _⊕										
3000	60	0.026R _*	0.026R _*	0.026R _*	0.026R _*	0.026R _*	0.026R _*	0.035R _*	0.035R _*	0.035R _*
3000	100	0.026R _*	0.026R _*	0.026R _*	0.026R _*	0.026R _*	0.026R _*	0.035R _*	0.035R _*	0.035R _*
3000	150	0.026R _*	0.026R _*	0.026R _*	0.035R _*	0.035R _*	0.026R _*	0.035R _*	0.035R _*	0.035R _*
3000	200	0.035R _*	0.035R _*	0.035R _*	0.035R _*	0.035R _*	0.035R _*	0.035R _*	0.035R _*	0.044R _*
3050	60	0.026R _*	0.026R _*	0.026R _*	0.035R _*	0.035R _*	0.035R _*	0.035R _*	0.035R _*	0.035R _*
3050	100	0.026R _*	0.026R _*	0.026R _*	0.035R _*	0.035R _*	0.035R _*	0.035R _*	0.035R _*	0.035R _*
3050	150	0.035R _*	0.035R _*	0.026R _*	0.035R _*	0.035R _*	0.035R _*	0.035R _*	0.035R _*	0.035R _*
3050	200	0.035R _*	0.035R _*	0.035R _*	0.044R _*	0.035R _*	0.035R _*	0.044R _*	0.044R _*	0.044R _*
3100	60	0.035R _*	0.035R _*	0.035R _*	0.035R _*	0.035R _*	0.035R _*	0.044R _*	0.044R _*	0.044R _*
3100	100	0.035R _*	0.035R _*	0.035R _*	0.035R _*	0.035R _*	0.035R _*	0.044R _*	0.044R _*	0.044R _*
3100	150	0.035R _*	0.035R _*	0.035R _*	0.044R _*	0.044R _*	0.044R _*	0.044R _*	0.044R _*	0.052R _*
3100	200	0.044R _*	0.044R _*	0.044R _*	0.044R _*	0.044R _*	0.052R _*	0.052R _*	0.052R _*	0.052R _*
3150	60	0.044R _*	0.044R _*	0.052R _*	0.052R _*	0.052R _*	0.052R _*	0.061R _*	0.061R _*	0.061R _*
3150	100	0.044R _*	0.044R _*	0.052R _*	0.052R _*	0.052R _*	0.052R _*	0.061R _*	0.061R _*	0.061R _*
3150	150	0.052R _*	0.052R _*	0.052R _*	0.052R _*	0.052R _*	0.061R _*	0.061R _*	0.061R _*	0.061R _*
3150	200	0.052R _*	0.061R _*	0.061R _*	0.061R _*	0.070R _*	0.070R _*	0.070R _*	0.070R _*	0.079R _*
R _p = 2.25R _⊕										
3000	60	0.026R _*	0.026R _*	0.026R _*	0.035R _*	0.035R _*	0.035R _*	0.035R _*	0.035R _*	0.035R _*
3000	100	0.026R _*	0.026R _*	0.026R _*	0.035R _*	0.035R _*	0.035R _*	0.035R _*	0.035R _*	0.035R _*
3000	150	0.026R _*	0.026R _*	0.026R _*	0.035R _*	0.035R _*	0.035R _*	0.035R _*	0.035R _*	0.035R _*
3000	200	0.035R _*	0.035R _*	0.035R _*	0.035R _*	0.035R _*	0.035R _*	0.035R _*	0.044R _*	0.044R _*
3050	60	0.035R _*	0.035R _*	0.035R _*	0.035R _*	0.035R _*	0.035R _*	0.044R _*	0.044R _*	0.044R _*
3050	100	0.035R _*	0.035R _*	0.035R _*	0.035R _*	0.035R _*	0.035R _*	0.044R _*	0.044R _*	0.044R _*
3050	150	0.035R _*	0.035R _*	0.035R _*	0.035R _*	0.035R _*	0.035R _*	0.044R _*	0.044R _*	0.044R _*
3050	200	0.035R _*	0.035R _*	0.035R _*	0.044R _*	0.044R _*	0.044R _*	0.044R _*	0.044R _*	0.044R _*
3100	60	0.044R _*	0.044R _*	0.044R _*	0.044R _*	0.044R _*	0.044R _*	0.044R _*	0.044R _*	0.044R _*
3100	100	0.044R _*	0.044R _*	0.044R _*	0.044R _*	0.044R _*	0.044R _*	0.044R _*	0.044R _*	0.044R _*
3100	150	0.044R _*	0.044R _*	0.044R _*	0.044R _*	0.044R _*	0.044R _*	0.044R _*	0.044R _*	0.044R _*
3100	200	0.044R _*	0.044R _*	0.044R _*	0.044R _*	0.044R _*	0.044R _*	0.052R _*	0.052R _*	0.052R _*
3150	60	0.052R _*	0.052R _*	0.052R _*	0.061R _*	0.061R _*	0.061R _*	0.061R _*	0.061R _*	0.070R _*
3150	100	0.052R _*	0.052R _*	0.052R _*	0.061R _*	0.061R _*	0.061R _*	0.061R _*	0.061R _*	0.070R _*
3150	150	0.052R _*	0.052R _*	0.052R _*	0.061R _*	0.061R _*	0.061R _*	0.061R _*	0.061R _*	0.070R _*
3150	200	0.061R _*	0.061R _*	0.061R _*	0.061R _*	0.070R _*	0.070R _*	0.070R _*	0.070R _*	0.079R _*
R _p = 2.50R _⊕										
3000	60	0.035R _*	0.035R _*	0.035R _*	0.035R _*	0.035R _*	0.035R _*	0.044R _*	0.044R _*	0.044R _*
3000	100	0.035R _*	0.035R _*	0.035R _*	0.035R _*	0.035R _*	0.035R _*	0.044R _*	0.044R _*	0.044R _*
3000	150	0.035R _*	0.035R _*	0.035R _*	0.035R _*	0.035R _*	0.035R _*	0.044R _*	0.044R _*	0.044R _*
3000	200	0.035R _*	0.035R _*	0.035R _*	0.035R _*	0.035R _*	0.035R _*	0.044R _*	0.044R _*	0.044R _*
3050	60	0.035R _*	0.035R _*	0.035R _*	0.044R _*	0.044R _*	0.044R _*	0.044R _*	0.044R _*	0.044R _*
3050	100	0.035R _*	0.035R _*	0.035R _*	0.044R _*	0.044R _*	0.044R _*	0.044R _*	0.044R _*	0.044R _*
3050	150	0.035R _*	0.035R _*	0.035R _*	0.044R _*	0.044R _*	0.044R _*	0.044R _*	0.044R _*	0.044R _*
3050	200	0.035R _*	0.035R _*	0.035R _*	0.044R _*	0.044R _*	0.044R _*	0.044R _*	0.044R _*	0.044R _*
3100	60	0.044R _*	0.044R _*	0.044R _*	0.044R _*	0.044R _*	0.044R _*	0.052R _*	0.052R _*	0.052R _*
3100	100	0.044R _*	0.044R _*	0.044R _*	0.044R _*	0.044R _*	0.044R _*	0.052R _*	0.052R _*	0.052R _*
3100	150	0.044R _*	0.044R _*	0.044R _*	0.044R _*	0.044R _*	0.044R _*	0.052R _*	0.052R _*	0.052R _*
3100	200	0.044R _*	0.044R _*	0.044R _*	0.044R _*	0.044R _*	0.044R _*	0.052R _*	0.052R _*	0.052R _*
3150	60	0.052R _*	0.052R _*	0.052R _*	0.061R _*	0.061R _*	0.061R _*	0.070R _*	0.070R _*	0.070R _*
3150	100	0.052R _*	0.052R _*	0.052R _*	0.061R _*	0.061R _*	0.061R _*	0.070R _*	0.070R _*	0.070R _*
3150	150	0.052R _*	0.052R _*	0.052R _*	0.061R _*	0.061R _*	0.061R _*	0.070R _*	0.070R _*	0.070R _*
3150	200	0.052R _*	0.052R _*	0.061R _*	0.061R _*	0.061R _*	0.061R _*	0.070R _*	0.070R _*	0.070R _*

$R_p = 2.75 R_\oplus$										
3000	60	0.035 R_*	0.035 R_*	0.035 R_*	0.035 R_*	0.035 R_*	0.035 R_*	0.044 R_*	0.044 R_*	0.044 R_*
3000	100	0.035 R_*	0.035 R_*	0.035 R_*	0.035 R_*	0.035 R_*	0.035 R_*	0.044 R_*	0.044 R_*	0.044 R_*
3000	150	0.035 R_*	0.035 R_*	0.035 R_*	0.035 R_*	0.035 R_*	0.035 R_*	0.044 R_*	0.044 R_*	0.044 R_*
3000	200	0.035 R_*	0.035 R_*	0.035 R_*	0.035 R_*	0.035 R_*	0.035 R_*	0.044 R_*	0.044 R_*	0.044 R_*
3050	60	0.035 R_*	0.035 R_*	0.035 R_*	0.044 R_*	0.044 R_*	0.044 R_*	0.044 R_*	0.044 R_*	0.044 R_*
3050	100	0.035 R_*	0.035 R_*	0.035 R_*	0.044 R_*	0.044 R_*	0.044 R_*	0.044 R_*	0.044 R_*	0.044 R_*
3050	150	0.035 R_*	0.035 R_*	0.035 R_*	0.044 R_*	0.044 R_*	0.044 R_*	0.044 R_*	0.044 R_*	0.044 R_*
3050	200	0.035 R_*	0.035 R_*	0.035 R_*	0.044 R_*	0.044 R_*	0.044 R_*	0.044 R_*	0.044 R_*	0.044 R_*
3100	60	0.044 R_*	0.044 R_*	0.044 R_*	0.052 R_*	0.052 R_*	0.052 R_*	0.052 R_*	0.052 R_*	0.052 R_*
3100	100	0.044 R_*	0.044 R_*	0.044 R_*	0.052 R_*	0.052 R_*	0.052 R_*	0.052 R_*	0.052 R_*	0.052 R_*
3100	150	0.044 R_*	0.044 R_*	0.044 R_*	0.052 R_*	0.052 R_*	0.052 R_*	0.052 R_*	0.052 R_*	0.052 R_*
3100	200	0.044 R_*	0.044 R_*	0.044 R_*	0.052 R_*	0.052 R_*	0.052 R_*	0.052 R_*	0.052 R_*	0.052 R_*
3150	60	0.061 R_*	0.061 R_*	0.061 R_*	0.070 R_*	0.070 R_*	0.070 R_*	0.079 R_*	0.079 R_*	0.079 R_*
3150	100	0.061 R_*	0.061 R_*	0.061 R_*	0.070 R_*	0.070 R_*	0.070 R_*	0.079 R_*	0.079 R_*	0.079 R_*
3150	150	0.061 R_*	0.061 R_*	0.061 R_*	0.070 R_*	0.070 R_*	0.070 R_*	0.079 R_*	0.079 R_*	0.079 R_*
3150	200	0.061 R_*	0.061 R_*	0.061 R_*	0.070 R_*	0.070 R_*	0.070 R_*	0.079 R_*	0.079 R_*	0.079 R_*
$R_p = 3.00 R_\oplus$										
3000	60	0.035 R_*	0.035 R_*	0.035 R_*	0.044 R_*	0.044 R_*	0.044 R_*	0.044 R_*	0.044 R_*	0.044 R_*
3000	100	0.035 R_*	0.035 R_*	0.035 R_*	0.044 R_*	0.044 R_*	0.044 R_*	0.044 R_*	0.044 R_*	0.044 R_*
3000	150	0.035 R_*	0.035 R_*	0.035 R_*	0.044 R_*	0.044 R_*	0.044 R_*	0.044 R_*	0.044 R_*	0.044 R_*
3000	200	0.035 R_*	0.035 R_*	0.035 R_*	0.044 R_*	0.044 R_*	0.044 R_*	0.044 R_*	0.044 R_*	0.044 R_*
3050	60	0.044 R_*	0.044 R_*	0.044 R_*	0.044 R_*	0.044 R_*	0.044 R_*	0.052 R_*	0.052 R_*	0.052 R_*
3050	100	0.044 R_*	0.044 R_*	0.044 R_*	0.044 R_*	0.044 R_*	0.044 R_*	0.052 R_*	0.052 R_*	0.052 R_*
3050	150	0.044 R_*	0.044 R_*	0.044 R_*	0.044 R_*	0.044 R_*	0.044 R_*	0.052 R_*	0.052 R_*	0.052 R_*
3050	200	0.044 R_*	0.044 R_*	0.044 R_*	0.044 R_*	0.044 R_*	0.044 R_*	0.052 R_*	0.052 R_*	0.052 R_*
3100	60	0.052 R_*	0.052 R_*	0.052 R_*	0.052 R_*	0.052 R_*	0.052 R_*	0.061 R_*	0.061 R_*	0.061 R_*
3100	100	0.052 R_*	0.052 R_*	0.052 R_*	0.052 R_*	0.052 R_*	0.052 R_*	0.061 R_*	0.061 R_*	0.061 R_*
3100	150	0.052 R_*	0.052 R_*	0.052 R_*	0.052 R_*	0.052 R_*	0.052 R_*	0.061 R_*	0.061 R_*	0.061 R_*
3100	200	0.052 R_*	0.052 R_*	0.052 R_*	0.052 R_*	0.052 R_*	0.052 R_*	0.061 R_*	0.061 R_*	0.061 R_*
3150	60	0.070 R_*	0.070 R_*	0.070 R_*	0.079 R_*	0.079 R_*	0.079 R_*	0.087 R_*	0.087 R_*	0.087 R_*
3150	100	0.070 R_*	0.070 R_*	0.070 R_*	0.079 R_*	0.079 R_*	0.079 R_*	0.087 R_*	0.087 R_*	0.087 R_*
3150	150	0.070 R_*	0.070 R_*	0.070 R_*	0.079 R_*	0.079 R_*	0.079 R_*	0.087 R_*	0.087 R_*	0.087 R_*
3150	200	0.070 R_*	0.070 R_*	0.070 R_*	0.079 R_*	0.079 R_*	0.079 R_*	0.087 R_*	0.087 R_*	0.087 R_*

Table A.2. The smallest detectable value of r_{spot} determined from the 7812 simulations of the 1296 scenarios that used an M1V dwarf host star. For a direct comparison with the results from the M4V dwarf host star simulations, the values of r_{spot} in brackets are the starspot size if they were on the M4V dwarf.

[illegible]

[illegible]

[illegible]

Table A.3. The smallest detectable value of r_{spot} determined from the 6737 simulations of the 1296 scenarios that used an K5V dwarf host star. For a direct comparison with the results from the M4V dwarf host star simulations, the values of r_{spot} in brackets are the starspot size if they were on the M4V dwarf.

T_{spot} (K)	rms scatter (ppm)	$\lambda_{\text{obs}} = 600 \text{ nm}$			$\lambda_{\text{obs}} = 785 \text{ nm}$			$\lambda_{\text{obs}} = 1000 \text{ nm}$		
		P			P			P		
		2 d	4 d	6 d	2 d	4 d	6 d	2 d	4 d	6 d
$R_p = 3.00 R_{\oplus}$										
3700	60	0.017 R_* (0.070 R_*)	0.017 R_* (0.070 R_*)	0.026 R_* (0.105 R_*)	0.017 R_* (0.070 R_*)	0.017 R_* (0.070 R_*)	0.026 R_* (0.105 R_*)	0.017 R_* (0.070 R_*)	0.026 R_* (0.105 R_*)	0.026 R_* (0.105 R_*)
3700	100	0.026 R_* (0.105 R_*)	0.026 R_* (0.105 R_*)	0.026 R_* (0.105 R_*)	0.026 R_* (0.105 R_*)	0.026 R_* (0.105 R_*)	0.035 R_* (0.140 R_*)	0.026 R_* (0.105 R_*)	0.035 R_* (0.140 R_*)	0.035 R_* (0.140 R_*)
3700	150	0.026 R_* (0.105 R_*)	0.035 R_* (0.140 R_*)	0.035 R_* (0.140 R_*)	0.026 R_* (0.105 R_*)	0.035 R_* (0.140 R_*)	0.035 R_* (0.140 R_*)	0.035 R_* (0.140 R_*)	0.035 R_* (0.140 R_*)	0.044 R_* (0.175 R_*)
3700	200	0.035 R_* (0.140 R_*)	0.035 R_* (0.140 R_*)	0.044 R_* (0.175 R_*)	0.035 R_* (0.140 R_*)	0.035 R_* (0.140 R_*)	0.044 R_* (0.175 R_*)	0.035 R_* (0.140 R_*)	0.044 R_* (0.175 R_*)	0.044 R_* (0.175 R_*)
3800	60	0.017 R_* (0.070 R_*)	0.017 R_* (0.070 R_*)	0.026 R_* (0.105 R_*)	0.017 R_* (0.070 R_*)	0.026 R_* (0.105 R_*)	0.026 R_* (0.105 R_*)	0.026 R_* (0.105 R_*)	0.026 R_* (0.105 R_*)	0.026 R_* (0.105 R_*)
3800	100	0.026 R_* (0.105 R_*)	0.026 R_* (0.105 R_*)	0.035 R_* (0.140 R_*)	0.026 R_* (0.105 R_*)	0.035 R_* (0.140 R_*)	0.035 R_* (0.140 R_*)	0.026 R_* (0.105 R_*)	0.035 R_* (0.140 R_*)	0.044 R_* (0.175 R_*)
3800	150	0.026 R_* (0.105 R_*)	0.035 R_* (0.140 R_*)	0.035 R_* (0.140 R_*)	0.035 R_* (0.140 R_*)	0.044 R_* (0.175 R_*)	0.044 R_* (0.175 R_*)	0.035 R_* (0.140 R_*)	0.044 R_* (0.175 R_*)	0.052 R_* (0.209 R_*)
3800	200	0.035 R_* (0.140 R_*)	0.035 R_* (0.140 R_*)	0.044 R_* (0.175 R_*)	0.044 R_* (0.175 R_*)	0.044 R_* (0.175 R_*)	0.052 R_* (0.209 R_*)	0.044 R_* (0.175 R_*)	0.052 R_* (0.209 R_*)	0.061 R_* (0.244 R_*)
3900	60	0.017 R_* (0.070 R_*)	0.026 R_* (0.105 R_*)	0.026 R_* (0.105 R_*)	0.026 R_* (0.105 R_*)	0.026 R_* (0.105 R_*)	0.035 R_* (0.140 R_*)	0.026 R_* (0.105 R_*)	0.026 R_* (0.105 R_*)	0.035 R_* (0.140 R_*)
3900	100	0.026 R_* (0.105 R_*)	0.035 R_* (0.140 R_*)	0.035 R_* (0.140 R_*)	0.035 R_* (0.140 R_*)	0.035 R_* (0.140 R_*)	0.044 R_* (0.175 R_*)	0.035 R_* (0.140 R_*)	0.044 R_* (0.175 R_*)	0.052 R_* (0.209 R_*)
3900	150	0.035 R_* (0.140 R_*)	0.044 R_* (0.175 R_*)	0.044 R_* (0.175 R_*)	0.044 R_* (0.175 R_*)	0.044 R_* (0.175 R_*)	0.061 R_* (0.244 R_*)	0.044 R_* (0.175 R_*)	0.061 R_* (0.244 R_*)	0.070 R_* (0.279 R_*)
3900	200	0.044 R_* (0.175 R_*)	0.052 R_* (0.209 R_*)	0.061 R_* (0.244 R_*)	0.052 R_* (0.209 R_*)	0.061 R_* (0.244 R_*)	0.079 R_* (0.314 R_*)	0.061 R_* (0.244 R_*)	0.079 R_* (0.314 R_*)	0.087 R_* (0.349 R_*)
4000	60	0.026 R_* (0.105 R_*)	0.035 R_* (0.140 R_*)	0.035 R_* (0.140 R_*)	0.035 R_* (0.140 R_*)	0.035 R_* (0.140 R_*)	0.044 R_* (0.175 R_*)	0.035 R_* (0.140 R_*)	0.044 R_* (0.175 R_*)	0.044 R_* (0.175 R_*)
4000	100	0.044 R_* (0.175 R_*)	0.044 R_* (0.175 R_*)	0.052 R_* (0.209 R_*)	0.044 R_* (0.175 R_*)	0.061 R_* (0.244 R_*)	0.070 R_* (0.279 R_*)	0.061 R_* (0.244 R_*)	0.079 R_* (0.314 R_*)	0.096 R_* (0.384 R_*)
4000	150	0.052 R_* (0.209 R_*)	0.070 R_* (0.279 R_*)	0.079 R_* (0.314 R_*)	0.183 R_* (0.733 R_*)	0.140 R_* (0.559 R_*)	0.271 R_* (1.082 R_*)	NaN	NaN	NaN
4000	200	NaN	NaN	NaN	NaN	NaN	NaN	NaN	NaN	NaN
$R_p = 3.50 R_{\oplus}$										
3700	60	0.017 R_* (0.070 R_*)	0.017 R_* (0.070 R_*)	0.017 R_* (0.070 R_*)	0.017 R_* (0.070 R_*)	0.017 R_* (0.070 R_*)	0.026 R_* (0.105 R_*)	0.017 R_* (0.070 R_*)	0.017 R_* (0.070 R_*)	0.026 R_* (0.105 R_*)
3700	100	0.017 R_* (0.070 R_*)	0.026 R_* (0.105 R_*)	0.026 R_* (0.105 R_*)	0.026 R_* (0.105 R_*)	0.026 R_* (0.105 R_*)	0.026 R_* (0.105 R_*)	0.026 R_* (0.105 R_*)	0.026 R_* (0.105 R_*)	0.035 R_* (0.140 R_*)
3700	150	0.026 R_* (0.105 R_*)	0.026 R_* (0.105 R_*)	0.035 R_* (0.140 R_*)	0.026 R_* (0.105 R_*)	0.035 R_* (0.140 R_*)	0.035 R_* (0.140 R_*)	0.035 R_* (0.140 R_*)	0.035 R_* (0.140 R_*)	0.035 R_* (0.140 R_*)
3700	200	0.035 R_* (0.140 R_*)	0.035 R_* (0.140 R_*)	0.035 R_* (0.140 R_*)	0.035 R_* (0.140 R_*)	0.035 R_* (0.140 R_*)	0.044 R_* (0.175 R_*)	0.035 R_* (0.140 R_*)	0.044 R_* (0.175 R_*)	0.044 R_* (0.175 R_*)
3800	60	0.017 R_* (0.070 R_*)	0.017 R_* (0.070 R_*)	0.026 R_* (0.105 R_*)	0.017 R_* (0.070 R_*)	0.017 R_* (0.070 R_*)	0.026 R_* (0.105 R_*)	0.017 R_* (0.070 R_*)	0.026 R_* (0.105 R_*)	0.026 R_* (0.105 R_*)
3800	100	0.026 R_* (0.105 R_*)	0.026 R_* (0.105 R_*)	0.026 R_* (0.105 R_*)	0.026 R_* (0.105 R_*)	0.026 R_* (0.105 R_*)	0.035 R_* (0.140 R_*)	0.026 R_* (0.105 R_*)	0.035 R_* (0.140 R_*)	0.035 R_* (0.140 R_*)
3800	150	0.026 R_* (0.105 R_*)	0.035 R_* (0.140 R_*)	0.035 R_* (0.140 R_*)	0.035 R_* (0.140 R_*)	0.035 R_* (0.140 R_*)	0.044 R_* (0.175 R_*)	0.035 R_* (0.140 R_*)	0.044 R_* (0.175 R_*)	0.044 R_* (0.175 R_*)
3800	200	0.035 R_* (0.140 R_*)	0.035 R_* (0.140 R_*)	0.044 R_* (0.175 R_*)	0.035 R_* (0.140 R_*)	0.044 R_* (0.175 R_*)	0.044 R_* (0.175 R_*)	0.044 R_* (0.175 R_*)	0.044 R_* (0.175 R_*)	0.052 R_* (0.209 R_*)
3900	60	0.017 R_* (0.070 R_*)	0.026 R_* (0.105 R_*)	0.026 R_* (0.105 R_*)	0.026 R_* (0.105 R_*)	0.026 R_* (0.105 R_*)	0.026 R_* (0.105 R_*)	0.026 R_* (0.105 R_*)	0.026 R_* (0.105 R_*)	0.035 R_* (0.140 R_*)
3900	100	0.026 R_* (0.105 R_*)	0.035 R_* (0.140 R_*)	0.035 R_* (0.140 R_*)	0.035 R_* (0.140 R_*)	0.035 R_* (0.140 R_*)	0.044 R_* (0.175 R_*)	0.035 R_* (0.140 R_*)	0.044 R_* (0.175 R_*)	0.044 R_* (0.175 R_*)
3900	150	0.035 R_* (0.140 R_*)	0.035 R_* (0.140 R_*)	0.044 R_* (0.175 R_*)	0.035 R_* (0.140 R_*)	0.044 R_* (0.175 R_*)	0.052 R_* (0.209 R_*)	0.044 R_* (0.175 R_*)	0.052 R_* (0.209 R_*)	0.061 R_* (0.244 R_*)
3900	200	0.035 R_* (0.140 R_*)	0.044 R_* (0.175 R_*)	0.052 R_* (0.209 R_*)	0.044 R_* (0.175 R_*)	0.052 R_* (0.209 R_*)	0.061 R_* (0.244 R_*)	0.052 R_* (0.209 R_*)	0.061 R_* (0.244 R_*)	0.070 R_* (0.279 R_*)
4000	60	0.026 R_* (0.105 R_*)	0.026 R_* (0.105 R_*)	0.035 R_* (0.140 R_*)	0.035 R_* (0.140 R_*)	0.035 R_* (0.140 R_*)	0.035 R_* (0.140 R_*)	0.035 R_* (0.140 R_*)	0.035 R_* (0.140 R_*)	0.044 R_* (0.175 R_*)
4000	100	0.035 R_* (0.140 R_*)	0.044 R_* (0.175 R_*)	0.052 R_* (0.209 R_*)	0.044 R_* (0.175 R_*)	0.052 R_* (0.209 R_*)	0.052 R_* (0.209 R_*)	0.052 R_* (0.209 R_*)	0.052 R_* (0.209 R_*)	0.061 R_* (0.244 R_*)
4000	150	0.052 R_* (0.209 R_*)	0.052 R_* (0.209 R_*)	0.061 R_* (0.244 R_*)	0.061 R_* (0.244 R_*)	0.070 R_* (0.279 R_*)	0.079 R_* (0.314 R_*)	0.070 R_* (0.279 R_*)	0.087 R_* (0.349 R_*)	0.113 R_* (0.454 R_*)
4000	200	0.061 R_* (0.244 R_*)	0.070 R_* (0.279 R_*)	0.087 R_* (0.349 R_*)	0.175 R_* (0.698 R_*)	0.096 R_* (0.384 R_*)	0.122 R_* (0.489 R_*)	NaN	NaN	NaN
$R_p = 4.00 R_{\oplus}$										
3700	60	0.017 R_* (0.070 R_*)	0.017 R_* (0.070 R_*)	0.017 R_* (0.070 R_*)	0.017 R_* (0.070 R_*)	0.017 R_* (0.070 R_*)	0.017 R_* (0.070 R_*)	0.017 R_* (0.070 R_*)	0.017 R_* (0.070 R_*)	0.026 R_* (0.105 R_*)
3700	100	0.026 R_* (0.105 R_*)	0.026 R_* (0.105 R_*)	0.026 R_* (0.105 R_*)	0.026 R_* (0.105 R_*)	0.026 R_* (0.105 R_*)	0.026 R_* (0.105 R_*)	0.026 R_* (0.105 R_*)	0.026 R_* (0.105 R_*)	0.026 R_* (0.105 R_*)
3700	150	0.026 R_* (0.105 R_*)	0.026 R_* (0.105 R_*)	0.026 R_* (0.105 R_*)	0.026 R_* (0.105 R_*)	0.026 R_* (0.105 R_*)	0.035 R_* (0.140 R_*)	0.026 R_* (0.105 R_*)	0.035 R_* (0.140 R_*)	0.035 R_* (0.140 R_*)
3700	200	0.026 R_* (0.105 R_*)	0.035 R_* (0.140 R_*)	0.035 R_* (0.140 R_*)	0.035 R_* (0.140 R_*)	0.035 R_* (0.140 R_*)	0.035 R_* (0.140 R_*)	0.035 R_* (0.140 R_*)	0.035 R_* (0.140 R_*)	0.044 R_* (0.175 R_*)
3800	60	0.017 R_* (0.070 R_*)	0.017 R_* (0.070 R_*)	0.017 R_* (0.070 R_*)	0.017 R_* (0.070 R_*)	0.017 R_* (0.070 R_*)	0.026 R_* (0.105 R_*)	0.017 R_* (0.070 R_*)	0.026 R_* (0.105 R_*)	0.026 R_* (0.105 R_*)
3800	100	0.026 R_* (0.105 R_*)	0.026 R_* (0.105 R_*)	0.026 R_* (0.105 R_*)	0.026 R_* (0.105 R_*)	0.026 R_* (0.105 R_*)	0.035 R_* (0.140 R_*)	0.026 R_* (0.105 R_*)	0.026 R_* (0.105 R_*)	0.035 R_* (0.140 R_*)
3800	150	0.026 R_* (0.105 R_*)	0.026 R_* (0.105 R_*)	0.035 R_* (0.140 R_*)	0.035 R_* (0.140 R_*)	0.035 R_* (0.140 R_*)	0.035 R_* (0.140 R_*)	0.035 R_* (0.140 R_*)	0.035 R_* (0.140 R_*)	0.044 R_* (0.175 R_*)
3800	200	0.035 R_* (0.140 R_*)	0.035 R_* (0.140 R_*)	0.035 R_* (0.140 R_*)	0.035 R_* (0.140 R_*)	0.035 R_* (0.140 R_*)	0.044 R_* (0.175 R_*)	0.035 R_* (0.140 R_*)	0.044 R_* (0.175 R_*)	0.044 R_* (0.175 R_*)
3900	60	0.017 R_* (0.070 R_*)	0.026 R_* (0.105 R_*)	0.026 R_* (0.105 R_*)	0.026 R_* (0.105 R_*)	0.026 R_* (0.105 R_*)	0.026 R_* (0.105 R_*)	0.026 R_* (0.105 R_*)	0.026 R_* (0.105 R_*)	0.026 R_* (0.105 R_*)
3900	100	0.026 R_* (0.105 R_*)	0.026 R_* (0.105 R_*)	0.035 R_* (0.140 R_*)	0.026 R_* (0.105 R_*)	0.035 R_* (0.140 R_*)	0.035 R_* (0.140 R_*)	0.035 R_* (0.140 R_*)	0.035 R_* (0.140 R_*)	0.044 R_* (0.175 R_*)
3900	150	0.035 R_* (0.140 R_*)	0.035 R_* (0.140 R_*)	0.044 R_* (0.175 R_*)	0.035 R_* (0.140 R_*)	0.044 R_* (0.175 R_*)	0.044 R_* (0.175 R_*)	0.044 $R_*</$		

[illegible]
$$R_p = 5.00 R_{\oplus}$$
[illegible]
$$R_p = 5.50 R_{\oplus}$$
[illegible]
$$R_p = 6.00 R_{\oplus}$$
[illegible]

[illegible]